

BOLTZSIM: A FAST SOLVER FOR THE 1D-SPACE ELECTRON BOLTZMANN EQUATION WITH APPLICATIONS TO RADIO-FREQUENCY GLOW DISCHARGE PLASMAS*

MILINDA FERNANDO[†], JAMES ALMGREN-BELL*, TODD OLIVER*, ROBERT MOSER*, PHILIP VARGHESE*, LAXMINARAYAN RAJA*, AND GEORGE BIROS*

Abstract. We present an algorithm for solving the one-dimensional space collisional Boltzmann transport equation (BTE) for electrons in low-temperature plasmas (LTPs). Modeling LTPs is useful in many applications, including advanced manufacturing, material processing, and hypersonic flows, to name a few. The proposed BTE solver is based on an Eulerian formulation. It uses Chebyshev collocation method in physical space and a combination of Galerkin and discrete ordinates in velocity space. We present self-convergence results and cross-code verification studies compared to an in-house particle-in-cell (PIC) direct simulation Monte Carlo (DSMC) code. BOLTZSIM is our open source implementation of the solver. Furthermore, we use BOLTZSIM to simulate radio-frequency glow discharge plasmas (RF-GDPs) and compare with an existing methodology that approximates the electron BTE. We compare these two approaches and quantify their differences as a function of the discharge pressure. The two approaches show an 80x, 3x, 1.6x, and 0.98x difference between cycle-averaged time periodic electron number density profiles at 0.1 Torr, 0.5 Torr, 1 Torr, and 2 Torr discharge pressures, respectively. As expected, these differences are significant at low pressures, for example less than 1 Torr.

Key words. Boltzmann equation, Galerkin approach, Multi-term expansion, Low-temperature plasma, glow discharge plasma

MSC codes. 35Q20, 82B40, 82D10

1. Introduction. Low-temperature plasmas (LTPs) find application in advanced manufacturing, semiconductor processing, the medical device industry, plasma-assisted combustion, and numerous other application domains. Modeling of low-temperature, weakly ionized plasmas can be challenging due to non-equilibrium chemistry, time-scale differences, and non-local electromagnetic coupling of charged particles. Electrons in LTPs often deviate from thermal equilibrium. Hence, their velocity space distribution functions differ from the Maxwell-Boltzmann distribution. Accurate modeling of LTPs requires solving the BTE for the electron distribution function (EDF). The BTE evolves the EDF dynamics and is coupled to ion and neutral species dynamics. Solving the BTE is a challenging task due to the dimensionality of the problem, the multiple time scales in various plasma processes, and dense collisional operators. Predictive simulation of LTPs relies on a hierarchy of models ranging from semi-analytical models to a fully kinetic treatment of plasma. Most existing LTP simulations rely on a model known as the “fluid approximation” that is derived from averaging the first three velocity space moments, mass, momentum, and energy of the BTE. The fluid approximation for the electron transport is based on assumptions on the EDF that may be invalid in certain LTP conditions. They also require approximating quantities that depend on the EDF, e.g., reaction rates, electron mobility, and electron diffusivity.

In this paper, we relax the fluid approximation for the electrons and discuss the

*Submitted to the editors February 23, 2025.

Funding: This work was funded by the U.S. Department of Energy, National Nuclear Security Administration award number DE-NA0003969

[†]Oden Institute, The University of Texas at Austin (milinda@oden.utexas.edu, jalmgrenbell@utexas.edu, oliver@oden.utexas.edu, rmoser@oden.utexas.edu, varghese@mail.utexas.edu, raja@mail.utexas.edu, biros@oden.utexas.edu).

numerical solution of the BTE in one spatial dimension and three velocity dimensions. We refer to this problem as the 1D3V BTE and the spatially homogeneous case as the 0D3V BTE. There are two main approaches for numerically solving the 1D3V BTE: Lagrangian and Eulerian. In the Lagrangian approach, a particle-in-cell (PIC) scheme is used for phase space advection, and the direct simulation Monte Carlo (DSMC) sampling approach is used to model particle collisions. In contrast, Eulerian solvers discretize the BTE in a fixed frame with standard PDE discretization techniques such as Galerkin, finite differences, and spectral methods. Eulerian BTE solvers are also referred to as deterministic BTE solvers because of the absence of sampling methods for particle collisions. In this paper, we focus on the Eulerian approach for solving spatially coupled electron BTE for LTPs. The developed methodology is applied to the kinetic treatment of electrons in low-temperature radio-frequency glow discharge plasmas (RF-GDPs). To our knowledge, existing work uses either PIC-DSMC or fluid approximations for RF-GDP simulations. We introduce a hybrid solver where the heavies are represented using a fluid approximation, and the electrons are by the BTE. We refer to the new solver as BOLTZSIM. Our contributions are summarized below.

- **Multi-term EDF approximation:** BOLTZSIM extends the traditional two-term EDF expansion with arbitrary multi-term EDF approximations for one-dimensional space electron BTE.
- **Semi-implicit and fully implicit schemes:** We present novel numerical schemes for the time evolution of electron BTE, with semi-implicit and fully-implicit coupling with the self-consistent electric field generated by charged plasma species. We propose a domain decomposition-based preconditioning method for the implicit time integration of the BTE for both semi and fully implicit schemes.
- **Self-consistent hybrid model for RF-GDPs:** We propose a self-consistent fluid and BTE combined hybrid transport model for RF-GDPs. We use the BTE for the kinetic treatment of electrons and the fluid approximation for heavy species transport.
- **Comparison between fluid and hybrid models:** A comparison between fluid and hybrid transport models is carried out for RF-GDPs, with argon ions and electrons. Using the RF-GDP setup, we verify our solver by comparing to an in-house PIC-DSMC code.
- **Open source:** Our solver is implemented in the Python programming language with support for CPU and portable GPU acceleration. The solver is openly available at <https://github.com/ut-padas/boltzmann>.

2. Background. We summarize existing methods for modeling GDPs. The fluid approximation is the most widely used approach to simulate RF-GDPs [3, 1, 29, 26, 25, 18, 11, 13]. There have been several attempts for the two-dimensional modeling of RF-GDPs using the fluid approximation [26, 24]. Lagrangian particle-in-cell algorithms for evolving fluid equations for GDPs are discussed in [26, 25]. The fluid approximation assumes that species distribution functions are isotropic. This is not the case, especially for the electrons closer to discharge walls due to a combination of boundary conditions and the strong electric field gradients in the sheath. Most BTE solvers are based on the PIC-DSMC approach [21, 28, 7, 17, 2, 16, 12]. There have been several attempts [22, 4, 20, 23, 27] to develop more accurate models for GDPs, specifically using the BTE for electrons. The authors in [22] use a PIC-DSMC approach to model species transport using the BTE but have limited details on the

collisional process. A hybrid modeling approach that uses the fluid approximation for heavies and the BTE for electrons is proposed in [4] using a PIC-DSMC to simulate the BTE effects. In [20] the authors propose a two-dimensional hybrid model for RF-GDPs by evolving the BTE with a simplified Bhatnagar–Gross–Krook (BGK) collision operator. A hybrid transport model with two-term EDF approximations is proposed in [27, 14]. The work given by [27] uses an approximation scheme to update the two EDF components, and the work by [14] uses a quasi-stationary approximation of the EDF with a simplified collision operator. Both of these works do not solve the one-dimensional electron BTE.

To the best of our knowledge, there has been limited work on spatially inhomogeneous Eulerian electron BTE solvers for LTPs as well as RF-GDPs. Also, the existing literature has limited discussion on solver algorithmic details and related complexity analysis for 1D3V LTP solvers. Our work is based on a Eulerian 0D3V BTE solver we developed in our group [6]. For related work please see the discussion in [6]. Here we focus on 1D3V solvers.

3. Methodology. This section presents an overview of the electron BTE (see Subsection 3.1) and its application to model electron transport in glow discharge devices (see Subsection 3.2). Table 3.1 summarizes the symbols used in the paper.

Symbol	Description	Symbol	Description
p_0	Gas pressure	T_0	Gas temperature
n_0	Neutral density	L	Electrode gap
V_0	Peak voltage	ζ	Oscillation frequency
D_e	Electron diffusion coefficient	D_i	Ion diffusion coefficient
μ_e	Electron mobility coefficient	μ_i	Ion mobility coefficient
T_e	Electron temperature	q_e	Electron charge
m_e	Electron mass	$f(\mathbf{x}, \mathbf{v}, t)$	EDF
\mathbf{E}	Electric field	N_x	Number of collocation points in x
N_r	Number of B-splines in v	N_{v_θ}	Number of ordinates in v_θ
N_l	Number of spherical harmonics in v_θ	\mathbf{C}_{en}	Discrete electron-neutral collision operator
\mathbf{A}_v	Discrete velocity space advection	\mathbf{D}_x	Spatial derivative operator (Chebyshev-collocation)
\mathbf{A}_x	Galerkin projection of $v \cos(v_\theta) \nabla_x f$ term	\mathbf{P}_S	v_θ ordinates to spherical harmonics projection
\mathbf{P}_O	Spherical harmonics to v_θ ordinates projection	\mathbf{F}	Discretized EDF
σ_0	Momentum transfer cross-section	σ_i	Ionization cross-section

Table 3.1: Notation

3.1. The electron Boltzmann transport equation (BTE). The electron BTE driven by an electric field $\mathbf{E}(\mathbf{x}, t)$ is given by

$$(3.1) \quad \partial_t f + \mathbf{v} \cdot \nabla_{\mathbf{x}} f - \frac{q_e \mathbf{E}}{m_e} \cdot \nabla_{\mathbf{v}} f = C_{en}(f).$$

Here, $f(\mathbf{x}, \mathbf{v}, t)$ denotes the EDF, $\mathbf{x} \in \Omega \subset \mathbb{R}^3$, $\mathbf{v} \in \mathbb{R}^3$ and $t \in \mathbb{R}$, and C_{en} denotes the electron-heavy binary collision operator. C_{en} comprises the electron-heavy momentum transfer and ionization collisions and $f(\mathbf{x}, \mathbf{v}, t) d\mathbf{x} d\mathbf{v}$ denotes the number of electrons for the phase-space volume $d\mathbf{x} d\mathbf{v}$. Using spherical coordinates $\mathbf{v} = (v, v_\theta, v_\varphi)$ in velocity space and aligning the velocity space z-axis to \mathbf{E} direction, we obtain $\mathbf{E} = E \hat{\mathbf{e}}_z = E(\cos(v_\theta) \hat{\mathbf{e}}_r - \sin(v_\theta) \hat{\mathbf{e}}_\theta)$. By restricting \mathbf{x} in 1D, we obtain the 1D3V BTE which is given by

$$(3.2) \quad [1D3V]: \quad \partial_t f + v \cos(v_\theta) \partial_x f - \frac{q_e E}{m_e} \left(\cos(v_\theta) \partial_v f - \sin(v_\theta) \frac{1}{v} \partial_{v_\theta} f \right) = C_{en}(f).$$

Furthermore, if we drop the spatial dependence entirely, we obtain the homogeneous 0D3V case, which is given by

$$(3.3) \quad [0D3V]: \quad \partial_t f - \frac{q_e E}{m_e} \left(\cos(v_\theta) \partial_v f - \sin(v_\theta) \frac{1}{v} \partial_{v_\theta} f \right) = C_{en}(f).$$

Electron-heavy collisions: The electron-heavy collision operator C_{en} captures the rate of change in the EDF due to collisions. It is given by

$$(3.4) \quad C_{en}^-(f, f_0) = \int_{\mathbb{R}^3} \int_{\mathbb{R}^3} \int_{S^2} B(\mathbf{v}'_e, \mathbf{v}'_0, \boldsymbol{\omega}) f(\mathbf{v}'_e) f_0(\mathbf{v}'_0) \delta(\mathbf{v}'_e - \mathbf{v}_e) d\mathbf{v}'_0 d\mathbf{v}'_e d\boldsymbol{\omega},$$

$$(3.5) \quad C_{en}^+(f, f_0) = \int_{\mathbb{R}^3} \int_{\mathbb{R}^3} \int_{S^2} B(\mathbf{v}'_e, \mathbf{v}'_0, \boldsymbol{\omega}) f(\mathbf{v}'_e) f_0(\mathbf{v}'_0) \delta(\mathbf{v}_e^{\text{post}}(\mathbf{v}'_e, \mathbf{v}'_0, \boldsymbol{\omega}) - \mathbf{v}_e) d\mathbf{v}'_0 d\mathbf{v}'_e d\boldsymbol{\omega},$$

$$(3.6) \quad C_{en}(f, f_0) = C_{en}^+(f, f_0) - C_{en}^-(f, f_0).$$

Here, f_0 denotes the heavy species distribution function, and B denotes the probability measure for a given collision parameters. The collision kernel B is defined by the collision cross-section [19]. These expressions can be further simplified by using the following common to LTPs assumptions: 1) The heavy species distribution functions are Maxwellian, and 2) electron-heavy collisions follow isotropic scattering. Here, the isotropic scattering assumption ensures that the collision probability measure is independent of the scattering angle. Under these assumptions, the BTE preserves the azimuthal symmetry in the velocity space. Equation (3.6) can be further simplified by assuming Maxwellian distribution for heavy species, i.e., $f_0(\mathbf{v}) = \frac{n_0}{(\sqrt{\pi}v_{th,0})^3} \exp\left(-v/v_{th,0}\right)^2$ where $v_{th,0} = \sqrt{2k_B T_0/m_0}$ is the thermal velocity, n_0 is the number density, and m_0 is the mass of the heavy species.

3.2. Glow discharge. Here, we summarize the formulation for RF-GDPs. An externally imposed potential difference between two electrodes at the opposite ends of a tube filled with argon is used to generate a plasma. Figure 3.1 shows a schematic of the glow discharge device. The imposed potential generates an electric field that

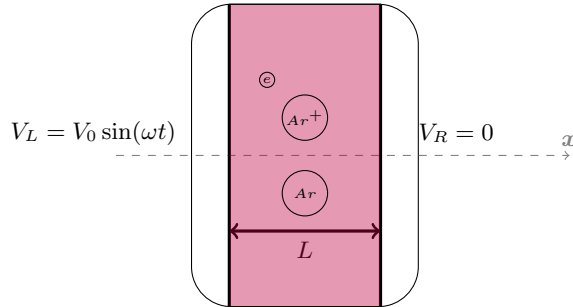


Fig. 3.1: An illustrative schematic for the glow discharge plasma with Argon.

causes electron acceleration and ionization of the background heavy species, which

results in the glow discharge plasma. Following standard approximations for GDPs, our formulation is based on the following assumptions:

1. We assume the size of the electrodes is larger than the discharge length (L). Hence, discharge characteristics vary along the normal direction to electrodes.
2. We limit our study to the three-species collisional model described in Table 3.2. We only consider direct ionization from the neutral state, ignoring excitation and step-ionization from metastable states. We remark that our solver easily extends to more species and collision types. Furthermore, assuming constant $n_0(x, t) = n_0$ value, we only track ions and electrons.
3. We assume heavies have constant temperature T_0 , typically the room temperature.
4. Following [13], we assume zero secondary electron emission from the electrode surface.

Collision	Threshold	Post-collision
$e + Ar \rightarrow e + Ar$	None	$\varepsilon_{\text{post}} = \varepsilon_{\text{pre}}(1 - \frac{2m_e}{m_0})$
$e + Ar \rightarrow Ar^+ + 2e$	$\varepsilon_{\text{ion}} = 15.76\text{eV}$	$\varepsilon_{\text{post}} = 0.5(\varepsilon_{\text{pre}} - \varepsilon_{\text{ion}})$

Table 3.2: Three species Ar collisional model.

We consider two formulations: In Subsection 3.2.1, we give a species transport formulation for the fluid approximation for both electrons and ions. In Subsection 3.2.2, we give the hybrid approximation where the fluid approximation describes ions, and the BTE models the electron transport. As mentioned, we assume constant neutral species density and temperature in both cases.

3.2.1. Fluid model for electrons and ions. We use a standard self-consistent fluid model for glow discharge phenomena [18, 13]. The species number density continuity equations are given by

$$(3.7a) \quad \partial_t n_e + \nabla \cdot \mathbf{J}_e = k_i n_0 n_e,$$

$$(3.7b) \quad \partial_t n_i + \nabla \cdot \mathbf{J}_i = k_i n_0 n_e.$$

Equations (3.7a) and (3.7b) describe the evolution of ions and electron number densities where k_i denotes the ionization rate coefficient, n_0 denotes the background neutral number density, and n_e denotes the electron number density. In Equation (3.7), flux terms, \mathbf{J}_e and \mathbf{J}_i are approximated using a drift-diffusion approximation [10] and are given by

$$(3.8) \quad \mathbf{J}_e = -\mu_e n_e \mathbf{E} - D_e \nabla n_e \quad \text{and} \quad \mathbf{J}_i = \mu_i n_i \mathbf{E} - D_i \nabla n_i.$$

The electron energy equation is given by

$$(3.9) \quad \partial_t \left(\frac{3}{2} n_e k T_e \right) = -\nabla \cdot \mathbf{q}_e - e \mathbf{J}_e \cdot \mathbf{E} - \varepsilon_{\text{ion}} k_i n_0 n_e,$$

and the electron energy flux term is specified by

$$(3.10) \quad \mathbf{q}_e = -\frac{3kD_e n_e}{2} \nabla T_e + \frac{5}{2} k T_e \mathbf{J}_e.$$

The underlying electric field potential is given by Gauss's law and given by

$$(3.11) \quad \Delta V = -\frac{e}{\epsilon_0}(n_i - n_e) \text{ and } \mathbf{E} = -\nabla V.$$

Boundary conditions: For electrons, we enforce the Maxwellian flux boundary condition [18] given by

$$(3.12) \quad \mathbf{J}_e \cdot \hat{\mathbf{n}} = \frac{1}{4}n_e \left(\frac{8k_B T_e}{\pi m_e} \right)^{0.5},$$

where $\hat{\mathbf{n}}$ is the outward unit normal vector. For the electron energy equation, the electron energy flux \mathbf{q}_e at the boundary is enforced to the average energy each electron carry when it escapes from the discharge walls and given by $\mathbf{q}_e = \frac{5}{2}k_B T_e \mathbf{J}_e$. For the ions, the enforced boundary condition is given by

$$(3.13) \quad \mathbf{J}_i \cdot \hat{\mathbf{n}} = -n_i \max(0, \mu_i \mathbf{E} \cdot \hat{\mathbf{n}}).$$

A Dirichlet condition for Equation (3.11) is given by the driving oscillatory voltage input

$$(3.14) \quad V(x=0, t) = V_0 \sin(2\pi\zeta t) \text{ and } V(x=L, t) = 0.$$

The fluid approximation for the glow discharge problem requires the kinetic coefficients, $\mu_{e,i}$, $D_{e,i}$ and k_i . Following [13], we use constant kinetic coefficients for the ions. For the electrons, we use temperature-based tabulated kinetic coefficients. Subsection 4.3 presents a detailed description of temperature-based electron kinetic coefficients. The fluid approximation for GDP simulation is summarized below.

$$\begin{aligned} (3.15a) & \quad \left. \begin{aligned} \partial_t n_i &= k_i(T_e)n_0 n_e - \nabla \cdot \mathbf{J}_i, \\ \partial_t n_e &= k_i(T_e)n_0 n_e - \nabla \cdot \mathbf{J}_e, \\ \partial_t \left(\frac{3}{2}n_e k T_e \right) &= -\nabla \cdot \mathbf{q}_e - e \mathbf{J}_e \cdot \mathbf{E} - \varepsilon_{\text{ion}} k_i(T_e)n_0 n_e, \\ \mathbf{J}_i &= \mu_i n_i \mathbf{E} - D_i \nabla n_i, \\ \mathbf{J}_e &= -\mu_e(T_e)n_e \mathbf{E} - D_e(T_e) \nabla n_e, \\ \mathbf{q}_e &= -\frac{3k D_e(T_e)n_e}{2} \nabla T_e + \frac{5}{2}k T_e \mathbf{J}_e, \\ \Delta V &= -\frac{e}{\epsilon_0}(n_i - n_e), \mathbf{E} = -\nabla V, \end{aligned} \right\} \\ (3.15b) & \\ (3.15c) & \\ (3.15d) \quad \forall t > 0, x \in [0, L] & \\ (3.15e) & \\ (3.15f) & \\ (3.15g) & \end{aligned}$$

$$\begin{aligned} (3.15h) & \quad \left. \begin{aligned} \mathbf{J}_i \cdot \hat{\mathbf{n}} &= -n_i \max(0, \mu_i \mathbf{E} \cdot \hat{\mathbf{n}}), \\ \mathbf{J}_e \cdot \hat{\mathbf{n}} &= \frac{1}{4}n_e \left(\frac{8k_B T_e}{\pi m_e} \right)^{1/2}, \\ \mathbf{q}_e &= \frac{5}{2}k_B T_e \mathbf{J}_e, \\ V(x=0, t) &= V_0 \sin(2\pi\zeta t), V(x=L, t) = 0. \end{aligned} \right\} \\ (3.15i) & \quad \forall t > 0, x=0 \text{ and } x=L \\ (3.15j) & \\ (3.15k) & \end{aligned}$$

3.2.2. Summary of the hybrid model. We replace Equations (3.15b), (3.15c), (3.15i), and (3.15j) with the 1D3V BTE. The combined equations become

$$\begin{aligned}
 (3.16a) \quad & \left\{ \begin{array}{l} \partial_t n_i + \nabla \cdot \mathbf{J}_i = k_i n_0 n_e, \\ \partial_t f + v \cos(v_\theta) \partial_x f - \\ (3.16b) \quad \frac{q_e E}{m_e} \left(\cos(v_\theta) \partial_v f - \sin(v_\theta) \frac{1}{v} \partial_{v_\theta} f \right) = C_{en}(f), \\ (3.16c) \quad \forall t > 0, x \in [0, L] \left\{ \begin{array}{l} \mathbf{J}_i = \mu_i n_i \mathbf{E} - D_i \nabla n_i, \\ (3.16d) \quad k_i = \int_{\mathbf{v}} \|\mathbf{v}\| \sigma_i \hat{f} d\mathbf{v} \text{ where } \hat{f}(\mathbf{v}) = \frac{f(\mathbf{v})}{\int_{\mathbf{v}} f(\mathbf{v}) d\mathbf{v}}, \\ (3.16e) \quad \Delta V = -\frac{e}{\epsilon_0} (n_i - n_e), \mathbf{E} = -\nabla V, \end{array} \right. \end{array} \right.
 \end{aligned}$$

$$\begin{aligned}
 (3.16f) \quad & \left\{ \begin{array}{l} \mathbf{J}_i \cdot \hat{\mathbf{n}} = -n_i \max(0, \mu_i \mathbf{E} \cdot \hat{\mathbf{n}}), \\ (3.16g) \quad \forall t > 0, x = 0 \text{ and } x = L \left\{ \begin{array}{l} f(x = 0, v, v_\theta \leq \frac{\pi}{2}, v_\varphi) = 0 \text{ and} \\ f(x = L, v, v_\theta > \frac{\pi}{2}, v_\varphi) = 0, \\ (3.16h) \quad V(x = 0, t) = V_0 \sin(2\pi\zeta t), V(x = L, t) = 0. \end{array} \right. \end{array} \right.
 \end{aligned}$$

Note that the EDF carries information on the electron number density $n_e(t, \mathbf{x}) = \int_{\mathbf{v}} f(t, \mathbf{x}, \mathbf{v}) d\mathbf{v}$ and σ_i denotes the total ionization cross section and \hat{f} denotes the normalized EDF. As prescribed above, we assume zero incoming flux boundary conditions for Equation (3.16b).

3.3. Numerical solver for the fluid approximation. As our focus is on the numerics of the hybrid solver, here we give a high-level description of the fluid solver. We are not claiming that this is the most efficient solver for this problem. Instead, we focus on comparing the converged time-periodic solutions between the fluid and the hybrid approaches. For the results of the fluid solver, we performed self-convergence tests in space and time. Now let us describe the solver for the fluid model described in Equation (3.15). We use a Chebyshev collocation method for the spatial discretization. These collocation points are clustered to the electrodes. This is ideal for efficiently resolving sharp gradients of the electric field, species densities, and the electron energy in the sheath. For the time discretization, we found that the operator-split approximation-based semi-implicit methods for solving Equations (3.15b), (3.15c), and (3.15g) have timestep size restrictions determined by the electron timescales (see Subsection 3.4.1). Therefore, the system given in Equation (3.15) is solved as a coupled non-linear system with fully implicit time integration. We use Newton's method with direct factorization of the assembled Jacobian to solve for the Newton step.

3.4. Hybrid fluid-BTE solver. Here, we discuss the discretization of Equation (3.16). First, let us consider the velocity space discretization of Equation (3.16b). The rate of change in the EDF due to the velocity space advection and collisions is given by Equation (3.3). For the velocity space, we use spherical coordinates with a mixed Galerkin and collocation scheme for the angular direction and a Galerkin

scheme for the radial coordinate discretization. We discretize $f(\mathbf{v}, t)$ as follows:

$$(3.17) \quad f(\mathbf{v}, t) = \sum_{klm} f_{klm}(t) \Phi_{klm}(\mathbf{v}) \quad \text{where} \quad \Phi_{klm}(\mathbf{v}) = \underbrace{\phi_k(v)}_{\text{B-Spline basis}} \overbrace{Y_{lm}(v_\theta, v_\phi)}^{\text{spherical harmonics}},$$

where $\left\{ \phi_k(v) \right\}_{k=0}^{N_r-1}$ are cubic B-splines defined on a regular grid, and $Y_{lm}(v_\theta, v_\phi)$ are defined as

$$(3.18) \quad Y_{lm}(v_\theta, v_\phi) = U_{lm} P_l^{|m|}(\cos(v_\theta)) \alpha_m(v_\phi),$$

$$U_{lm} = \begin{cases} (-1)^m \sqrt{2} \sqrt{\frac{2l+1}{4\pi} \frac{(l-|m|)!}{(l+|m|)!}}, & m \neq 0, \\ \sqrt{\frac{2l+1}{4\pi}}, & m = 0, \end{cases}, \quad \alpha_m(v_\phi) = \begin{cases} \sin(|m|\phi), & m < 0, \\ 1, & m = 0, \\ \cos(m\phi), & m > 0. \end{cases}$$

The l index is also referred to as a polar mode, and the m index as an azimuthal mode. Now, assume that $f_{klm}(t=0) = 0, \forall m > 0$. By aligning \mathbf{E} to the velocity space z-axis, so that $\mathbf{E} = E \hat{\mathbf{e}}_z = E(\cos(v_\theta) \hat{\mathbf{e}}_r - \sin(v_\theta) \hat{\mathbf{e}}_\theta)$ we ensure that the \mathbf{E} acceleration excites only the polar modes Equation (3.17). This fact and the isotropic scattering assumption ensure that the BTE solutions preserve the azimuthal symmetry in the velocity space and thus $f_{klm}(t)$ remains zero $\forall t > 0, m > 0$. This essentially reduces the representation from 1D3V to 1D2V. Therefore, the EDF representation only requires $\{Y_{l0}\}_l$ modes. For this reason, we drop the azimuthal index v_ϕ in the remainder of the paper. Let p, k denote the indices of the basis functions along the radial coordinate; q, l denote the indices in the polar angle; and $\phi_p(v), \phi_k(v)$ denote the test and trial B-splines in radial coordinate. Under these definitions, the discretized weak form of the collision operator is given by

$$(3.19) \quad n_0 [\mathbf{C}_{en}]_{kl}^{pq} = n_0 \int_{\mathbb{R}^+} v^2 \sigma_T(v) \phi_k(v) \delta_{ql} (\phi_p(u) \delta_{q0} - \phi_p(v)) dv,$$

for $p, k \in \{0, \dots, N_r - 1\}$ and $q, l \in \{0, \dots, N_l - 1\}$.

For non-zero heavy temperature, Equation (3.19) gets an additional correction term, given by

$$(3.20) \quad n_0 T_0 [\mathbf{C}_T]_{kl}^{pq} = \frac{n_0 T_0 k_B}{m_0} \delta_{q0} \int_{\mathbb{R}^+} v^3 \sigma_T(v) \partial_v \phi_p(v) \partial_v \phi_k(v) dv,$$

for $p, k \in \{0, \dots, N_r - 1\}$ and $q, l \in \{0, \dots, N_l - 1\}$.

In Equation (3.19) and Equation (3.20) σ_T denotes the total collisional cross-section, n_0 and T_0 denotes the background neutral density and temperature. In our case, we have momentum transfer and ionization collisions. For multiple collisions, the effective collision operator is given by $\mathbf{C}_{en}^{\text{effec.}} = \sum_{i \in \text{collisions}} n_i \mathbf{C}_{en}(\sigma_i) + n_0 T_0 \mathbf{C}_T(\sigma_0)$ where 0 index denotes the ground state heavy species, and σ_0 denotes the total cross-section for the momentum transfer collisions. The discretized velocity space acceleration

operator is given by

$$(3.21) \quad [\mathbf{A}_v]_{kl}^{pq} = \int_{\mathbb{R}^+} \delta_{(q+1)l} v^2 \phi_p(v) \left(A_M(l) \partial_v \phi_k(v) + A_D(l) \frac{1}{v} \phi_k(v) \right) + \delta_{(q-1)l} v^2 \phi_p(v) \left(B_M(l) \partial_v \phi_k(v) + B_D(l) \frac{1}{v} \phi_k(v) \right) dv, \\ \text{for } p, k \in \{0, \dots, N_r - 1\} \text{ and } q, l \in \{0, \dots, N_l - 1\},$$

where A_M , A_D , B_M , and B_D are coefficients defined by

$$(3.22) \quad A_M(l) = \frac{l}{\sqrt{4l^2 - 1}}, \quad B_M(l) = \frac{l+1}{\sqrt{4l^2 - 1}}, \quad A_D(l) = \frac{l^2}{\sqrt{4l^2 - 1}}, \quad B_D(l) = \frac{l(l-1)}{\sqrt{4l^2 - 1}}.$$

To summarize, the velocity space discretized BTE is given by

$$(3.23) \quad \partial_t (\mathbf{M}_{v, v_\theta} \mathbf{f}) = (\mathbf{C}_{en} + \mathbf{E} \mathbf{A}_v) \mathbf{f},$$

where \mathbf{M}_{v, v_θ} , \mathbf{C}_{en} , and $\mathbf{A}_v \in \mathbb{R}^{N_r N_l \times N_r N_l}$ denote the Galerkin mass matrix, electron-heavy collisions and the velocity space acceleration operators respectively. More details on the velocity space discretization can be found in [6].

Now we discuss the spatial discretization of Equation (3.16b). We use a Chebyshev collocation scheme for the spatial discretization of Equation (3.16b). The spherical harmonic representation is inadequate to impose the v_θ discontinuous boundary conditions specified in Equation (3.16g). This is resolved by a mixed Galerkin and collocation representation in v_θ . Let $\{x_i\}_{i=0}^{N_x-1}$ and $\{v_{\theta a}\}_{a=0}^{N_{v_\theta}-1}$ be collocation points in x , and v_θ coordinates. With these collocation points, the EDF representation is given by

$$(3.24) \quad f(x_i, v, v_{\theta a}, t) = \sum_{k=0}^{N_r-1} f_k(x_i, v_{\theta a}, t) \phi_k(v) = \sum_{k=0}^{N_r-1} f_{ika}(t) \phi_k(v), \\ \text{where } f_{ika}(t) \equiv f_k(x_i, v_{\theta a}, t),$$

and the semi-discrete form of Equation (3.16b) is given by

$$(3.25) \quad \partial_t f(t, x, v, v_{\theta a}) + v \cos(v_{\theta a}) \partial_x f(t, x, v, v_{\theta a}) = (\partial_t f)_{\mathbf{v}\text{-space}}(t, x, v, v_{\theta a}).$$

Let \mathbf{P}_S denotes the v_θ ordinates to spherical harmonics projection, and \mathbf{P}_O denotes the spherical harmonics to v_θ ordinates projection operators. These operators are defined by

$$(3.26) \quad \mathbf{P}_S = \mathbf{I}_v \otimes \mathbf{T}_S, \quad \mathbf{P}_O = \mathbf{I}_v \otimes \mathbf{T}_O \text{ where } [\mathbf{T}_S]_a^q = Y_q(v_{\theta a}) w_a \text{ and } [\mathbf{T}_O]_q^a = Y_q(v_{\theta a}), \text{ for } q \in \{0, \dots, N_l - 1\}, a \in \{0, \dots, N_{v_\theta} - 1\}.$$

Here, \otimes denotes the matrix Kronecker product, $\mathbf{I}_v \in \mathbb{R}^{N_r \times N_r}$ denotes the identity matrix in v coordinate, and w_a denotes the quadrature weights for the spherical basis projection. We use a Chebyshev collocation method in space, a Galerkin discretization in the v coordinate, and a mixed Galerkin and collocation scheme in the v_θ coordinate for the discretization of Equation (3.25). Let \mathbf{D}_x denotes the discrete Chebyshev-basis

derivative operator and \mathbf{A}_x denotes the v coordinate Galerkin projection of the spatial advection term in Equation (3.25). The \mathbf{A}_x operator is given by

$$(3.27) \quad \mathbf{A}_x = \mathbf{D}_{v_\theta} \otimes \mathbf{G}_v \text{ where, } [\mathbf{D}_{v_\theta}]_{ab} = \delta_{ab} \cos(v_{\theta a}) \text{ and}$$

$$[\mathbf{G}_v]_{pk} = \int_{\mathbb{R}^+} v^3 \phi_p(v) \phi_k(v) dv,$$

for $p, k \in \{0, \dots, N_r - 1\}$ and $a, b \in \{0, \dots, N_{v_\theta} - 1\}$.

By putting everything together, with x , v , and v_θ discretized BTE is given by

$$(3.28) \quad \partial_t \mathbf{F} + \mathbf{A}_x \mathbf{F} \mathbf{D}_x^T = \mathbf{P}_O \mathbf{C}_{en} \mathbf{P}_S \mathbf{F} + \mathbf{P}_O \mathbf{A}_v \mathbf{P}_S (\mathbf{E} \circ \mathbf{F}) \text{ where}$$

$$\mathbf{F} \in \mathbb{R}^{N_r N_{v_\theta} \times N_x}, \mathbf{P}_S \in \mathbb{R}^{N_r N_i \times N_r N_{v_\theta}},$$

$$\mathbf{C}_{en}, \mathbf{A}_v \in \mathbb{R}^{N_r N_i \times N_r N_i}, \mathbf{P}_O \in \mathbb{R}^{N_r N_{v_\theta} \times N_r N_i}, \mathbf{D}_x \in \mathbb{R}^{N_x \times N_x}, \mathbf{A}_x \in \mathbb{R}^{N_r N_{v_\theta} \times N_r N_{v_\theta}},$$

$$[\mathbf{F}]_{i,:} = f_{ika}, \text{ for } i \in \{0, \dots, N_x - 1\}, k \in \{0, \dots, N_r - 1\}, \text{ and } a \in \{0, \dots, N_{v_\theta} - 1\}.$$

Here, $\mathbf{E} \in \mathbb{R}^{N_x}$ and \circ denotes the column wise element product. Also, it is important to note that the operators in Equation (3.28) is properly scaled by Galerkin mass matrices, i.e., from here on, $\mathbf{G}_v \equiv \mathbf{M}_v^{-1} \mathbf{G}_v$, $\mathbf{A}_x \equiv \mathbf{D}_{v_\theta} \otimes \mathbf{G}_v$, $\mathbf{C}_{en} \equiv \mathbf{M}_{v, v_\theta}^{-1} \mathbf{C}_{en}$, and $\mathbf{A}_v \equiv \mathbf{M}_{v, v_\theta}^{-1} \mathbf{A}_v$, where \mathbf{M}_v and \mathbf{M}_{v, v_θ} denote the standard Galerkin mass matrices [5] in v and v, v_θ coordinates respectively. Equations (3.16a) and (3.16e) are discretized with the same Chebyshev collocation scheme we used for Equation (3.16b). Let $\mathbf{k}_i \in \mathbb{R}^{N_r N_{v_\theta}}$ denotes the discretized ionization rate coefficient operator, $\mathbf{u} \in \mathbb{R}^{N_r N_{v_\theta}}$ denotes the zeroth-order moment operator where $\mathbf{n}_e = \mathbf{u}^T \mathbf{F}$, and $\mathbf{L} \in \mathbb{R}^{N_x \times N_x}$ denotes the discretized electrostatics operator where $\mathbf{E} = \mathbf{L}(\mathbf{n}_i - \mathbf{n}_e)$. Then, the discretized hybrid model is given by

$$(3.29a) \quad \partial_t \mathbf{n}_i + \mathbf{D}_x \mathbf{J}_i(\mathbf{E}, \mathbf{n}_i) = \left(\mathbf{k}_i^T \mathbf{F} \right) n_0 \mathbf{n}_e,$$

$$(3.29b) \quad \partial_t \mathbf{F} + \mathbf{A}_x \mathbf{F} \mathbf{D}_x^T = \mathbf{P}_O \mathbf{C}_{en} \mathbf{P}_S \mathbf{F} + \mathbf{P}_O \mathbf{A}_v \mathbf{P}_S (\mathbf{E} \circ \mathbf{F}),$$

$$(3.29c) \quad \mathbf{E} = \mathbf{L}(\mathbf{n}_i - \mathbf{n}_e), \text{ where } \mathbf{n}_e = \mathbf{u}^T \mathbf{F}.$$

The total number of unknowns for the discretized system is $N_x(1 + N_r N_{v_\theta})$ where N_x , N_r , and N_{v_θ} denote the number of Chebyshev collocation points in x , the number of B-spline basis used in v , and the number of collocation points in v_θ .

3.4.1. Timescales analysis. Here, we present timescales analysis for Equation (3.29). Table 3.3 summarizes the main ion and electron timescales for a RF-GDP with $p_0 = 1$ Torr. The input voltage oscillation period is set to 7.374×10^{-8} s for all RF-GDP cases considered in this paper. The timescale for the collision operator is given by

$$(3.30) \quad \Delta t \frac{\|\mathbf{C}_{en} \mathbf{F}\|}{\|\mathbf{F}\|} \leq \Delta t \|\mathbf{C}_{en}\| \leq \Delta t n_0 \max(\|\mathbf{v}\| \sigma_0, \|\mathbf{v}\| \sigma_i) \leq \frac{\|\Delta \mathbf{F}\|}{\|\mathbf{F}\|}$$

$$\implies \Delta t \leq \frac{\|\Delta \mathbf{F}\|}{\|\mathbf{F}\|} \frac{1}{n_0 \max(\|\mathbf{v}\| \sigma_0, \|\mathbf{v}\| \sigma_i)} = \frac{\|\Delta \mathbf{F}\|}{\|\mathbf{F}\|} \frac{1}{n_0 \max(\|\mathbf{v}\| \sigma_0)}.$$

The reaction and collision terms determine the fastest timescale for ions and electrons. However, as shown in Table 3.3, ions have much slower timescales than electrons. Therefore, the electron timescale determines the electrostatic timescale. A change

in the electron number density $n_e(\mathbf{x}, t)$ is caused by the BTE spatial advection and reaction terms. While the velocity space advection is not directly coupled to $n_e(\mathbf{x}, t)$, it is indirectly coupled through the collision term. This is due to the EDF tails being populated due to the velocity space advection, and high-energy electrons are likely to trigger ionization collisions. Therefore, the electrostatic and the BTE coupling timescale is governed by the position-velocity space advection and the reaction term timescales. The collisional timescale gives the relative change in the EDF due to collisions. Typically, Since $\sigma_0 \geq \sigma_i$, the collisional timescale is determined by the momentum transfer cross-section.

Species	Term	Δt [s]
Ions	$\nabla_{\mathbf{x}} \cdot (\mu_i \mathbf{E} n_i)$ – advection	$\frac{\Delta x}{\mu_i \ \mathbf{E}_{\max}\ } \approx \mathcal{O}(10^{-9})$
	$\nabla_{\mathbf{x}} \cdot (D_i \nabla_{\mathbf{x}} n_i)$ – diffusion	$\frac{\Delta x^2}{2D_i} \approx \mathcal{O}(10^{-7})$
	$k_i n_0 n_e$ – reaction	$\frac{\Delta n_i}{n_i} \frac{n_i}{k_{i,\max} n_0 n_e} \approx \mathcal{O}(10^{-10})$
Electron BTE	$\mathbf{v} \cdot \nabla_{\mathbf{x}} f$ – \mathbf{x} -advection	$\frac{\Delta x}{\ \mathbf{v}\ } \approx \mathcal{O}(10^{-12})$
	$\frac{q_e \mathbf{E}}{m_e} \cdot \nabla_{\mathbf{v}} f$ – \mathbf{v} -advection	$\frac{\ \Delta \mathbf{v}\ m_e}{q_e \ \mathbf{E}_{\max}\ } \approx \mathcal{O}(10^{-12})$
	$k_i n_0 n_e = n_0 \int_{\mathbf{v}} \ \mathbf{v}\ ^3 \sigma_i(\ \mathbf{v}\) f(\mathbf{v}) d\mathbf{v}$ – reaction	$\frac{\Delta n_e}{n_e} \frac{1}{k_{i,\max} n_0} \approx \mathcal{O}(10^{-12})$
	$\mathbf{C}_{en} \mathbf{F}$ – collisions	$\frac{\ \Delta \mathbf{F}\ }{\ \mathbf{F}\ } \frac{1}{n_0 \max(\ \mathbf{v}\ \sigma_0)} \approx \mathcal{O}(10^{-13})$
Driving voltage	$V(t) = V_0 \sin(2\pi \zeta t)$	$1/\zeta = 7.374 \times 10^{-8}$

Table 3.3: A summary of the timescales for advection, diffusion, and reaction terms for the hybrid formulation, assuming an explicit time integration scheme. Here, we assume $\frac{\Delta x}{L} \approx \mathcal{O}(10^{-3})$, $\frac{\|\Delta \mathbf{v}\|}{\|\mathbf{v}\|} \approx \mathcal{O}(10^{-3})$, $\frac{\|\Delta \mathbf{F}\|}{\|\mathbf{F}\|} \approx \mathcal{O}(10^{-3})$, and $\frac{\Delta n_e}{n_e} \approx \mathcal{O}(10^{-3})$. The maximum absolute quantities occurs closer to the electrodes with $\|\mathbf{E}_{\max}\| = 8 \times 10^4$ [V/m], $k_{i,\max} = 10^{-14}$ [m^3/s], and the corresponding ionization degree $\frac{n_i}{n_e} \approx \mathcal{O}(10^2)$. For the other transport coefficients, we use the values summarized in Table 4.4 with the $p_0 = 1$ Torr case.

3.4.2. Hybrid solver time integration. Typically, we want to evolve the system to the order of thousand cycles or 10^{-5} seconds, and require ten million timesteps. An implicit scheme with an iterative solve is possible as the matrix-vector products can be also done in an optimal way, but designing a good preconditioner is not trivial. Instead we opt for an operator split scheme. As we can see in Table 3.3, the ions have slower timescales compared to electrons. Hence, we use an operator split scheme to decouple ion and electron transport equations. Since electrons determine the electrostatics coupling timescale, Equation (3.29a) is solved with decoupled electrostatics.

Heavies evolution: For a given state $(\mathbf{n}_i^n, \mathbf{F}^n)$ at time $t = t_n$, the ion transport equation is solved implicitly with lagged \mathbf{F}^n and $\mathbf{E}^n = \mathbf{L}(\mathbf{n}_i^n - \mathbf{u}^T \mathbf{F}^n)$. This coupling results in a linear system to be solved for the ions state at time $t_{n+1} = t_n + \Delta t$, where Δt denotes the time step size. So, the ions update in our operator-split scheme is given by

$$(3.31) \quad \frac{\mathbf{n}_i^{n+1} - \mathbf{n}_i^n}{\Delta t} + D_x \mathbf{J}_i(\mathbf{E}^n, \mathbf{n}_i^{n+1}) = (\mathbf{k}_i^T \mathbf{F}^n) n_0 (\mathbf{u}^T \mathbf{F}^n).$$

Electron evolution: We consider the evolution of Equations (3.29b) and (3.29c) assuming a fixed \mathbf{n}_i . We consider two alternative schemes for the electrons: a semi-implicit and a fully-implicit one. The semi-implicit scheme compute the EDF at time

$t + \Delta t$ is given by

$$(3.32a) \quad \begin{cases} \frac{\mathbf{F}^{n+1/2} - \mathbf{F}^n}{\Delta t/2} = -\mathbf{A}_x \mathbf{F}^{n+1/2} \mathbf{D}_x^T, t \in \left(t_n, t_n + \frac{\Delta t}{2}\right), \end{cases}$$

$$(3.32b) \quad \begin{cases} \mathbf{E}^{1/2} = \mathbf{L}(\mathbf{n}_i - \mathbf{u}^T \mathbf{F}^{n+1/2}), \end{cases}$$

$$(3.32c) \quad \begin{cases} \text{semi-implicit} \left\{ \begin{aligned} \frac{\mathbf{F}^* - \mathbf{F}^{n+1/2}}{\Delta t} &= \mathbf{P}_O \mathbf{C}_{en} \mathbf{P}_S \mathbf{F}^* + \\ &\mathbf{P}_O \mathbf{A}_v \mathbf{P}_S (\mathbf{E}^{1/2} \circledast \mathbf{F}^*), t \in (t_n, t_n + \Delta t), \end{aligned} \right. \end{cases}$$

$$(3.32d) \quad \begin{cases} \frac{\mathbf{F}^{n+1} - \mathbf{F}^*}{\Delta t/2} = -\mathbf{A}_x \mathbf{F}^{n+1} \mathbf{D}_x^T, t \in \left(t_{n+1/2}, t_{n+1/2} + \frac{\Delta t}{2}\right). \end{cases}$$

The overview of the semi-implicit scheme is summarized below.

- **Spatial advection:** Equations (3.32a) and (3.32d) corresponds to the spatial advection of electrons. We use the the eigen decomposition of $\mathbf{G}_v = \mathbf{U} \mathbf{\Lambda} \mathbf{U}^{-1}$ to diagonalize Equations (3.32a) and (3.32d). Since \mathbf{G}_v is a product of two positive definite matrices, it has real positive eigenvalues. Upon diagonalization, Equations (3.32a) and (3.32d) become series of decoupled $N_r N_{v_\theta}$ spatial advection equations where the advection velocity is given by $\mathbf{a} = \Lambda_i \cos(v_{\theta_j}) \hat{\mathbf{e}}_x$ for $i = \{0, \dots, N_r - 1\}$ and $j = \{0, \dots, N_{v_\theta} - 1\}$ where N_r and N_{v_θ} denotes the number of B-splines and v_θ ordinates used. For each i and j , we precompute and store the inverted $(\mathbf{I}_x + \frac{1}{2} \Delta t \Lambda_i \cos(v_{\theta_j}) \mathbf{D}_x)^{-1} = \mathbf{Q}_{ij}$ operators and use them for spatial advection. Here, $\mathbf{I}_x \in \mathbb{R}^{N_x \times N_x}$ denotes the identity matrix in the x dimension. This direct inversion is performed only once and reused throughout the time evolution. The storage cost for the inverted matrices is given by $\mathcal{O}(N_r N_{v_\theta} N_x^2)$. Algorithm 3.1 presents the overview of the BTE spatial advection step. In the implementation, the application of \mathbf{Q}_{ij} is performed as a batched general matrix-matrix multiplication (GEMM).
- **Electrostatics:** Equation (3.32b) computes the updated electric field $\mathbf{E}^{1/2}$ following the spatial advection. Here, $\mathbf{L} \in \mathbb{R}^{N_x \times N_x}$ denotes the discretized $\nabla_x \Delta_x^{-1}$ operator which is computed once and reused throughout the time evolution.
- **Velocity space update:** We use the generalized minimal residual method (GMRES) to solve Equation (3.32c). In Equation (3.32c), the discretized EDF is spatially decoupled, and the velocity space left-hand side operator varies spatially and is given by

$$(3.33) \quad \left(\mathbf{I}_{v,v_\theta} - \Delta t \mathbf{P}_O \left(\mathbf{C}_{en} + [\mathbf{E}^{1/2}]_i \mathbf{A}_v \right) \mathbf{P}_S \right) \mathbf{F}^* = \mathbf{F}^{n+1/2}$$

where $\mathbf{E}^{1/2} \in \mathbb{R}^{N_x}$, for $i \in \{0, \dots, N_x - 1\}$.

Here, \mathbf{I}_{v,v_θ} denotes the identity operator in the velocity space, and $[\mathbf{E}^{1/2}]_i$ denotes the electric field evaluated at the i -th spatial collocation point. Therefore, the solve of Equation (3.32c) reduces to a N_x decoupled linear systems. For the GMRES solve, these linear systems are solved as a batched system. The batched right-hand side evaluation is summarized in Algorithm 3.2. We use a domain decomposition preconditioner for the GMRES solve. Let E_0

denotes an upper bound on the electric field such that $\|\mathbf{E}(\mathbf{x}, t)\| \leq E_0 \forall t$ and $-E_0 = S_0 < S_1 < \dots < S_{N_c} = E_0$ be a time independent non-overlapping partition of $(-E_0, E_0)$. We precompute a series of operators $\{H_p\}_{p=1}^{N_c}$ where each $H_p \in \mathbb{R}^{N_r N_l}$ is given by

$$(3.34) \quad H_p = \left(\mathbf{I} - \Delta t \left(\mathbf{C}_{en} + \frac{1}{2} (S_{p-1} + S_p) \mathbf{A}_v \right) \right)^{-1} \quad \text{for } p \in \{1, \dots, N_c\}.$$

Here, $\mathbf{I} \in \mathbb{R}^{N_r N_l}$ denotes the identity matrix. For a specified $\mathbf{E} \in \mathbb{R}^{N_x}$, we define N_c partitions where partition w_k is given by $w_k = \{i \mid S_{k-1} \leq [\mathbf{E}]_i < S_k\}$ for $k \in \{1, \dots, N_c\}$. We refer to this as the preconditioner setup step, which is performed once per each timestep. The precondition operator evaluation is summarized in Algorithm 3.3.

Algorithm 3.1 BTE spatial advection.

Require: $\mathbf{F}^n \in \mathbb{R}^{N_r N_{v_\theta} \times N_x}$ – EDF at time t_n ,

- 1: $\left\{ \mathbf{Q}_{ij} = \left(\mathbf{I}_x + \frac{1}{2} \Delta t \Lambda_i \cos(v_{\theta j}) \mathbf{D}_x \right)^{-1} \right\}_{(i,j) \in \{0, \dots, N_r - 1\} \times \{0, \dots, N_{v_\theta} - 1\}}$ – inverted spatial advection operators, and $\mathbf{G}_v = \mathbf{U} \Lambda \mathbf{U}^{-1}$
 - Ensure:** Solution at time $t_n + \Delta t/2$, $\mathbf{F}^{1/2} \in \mathbb{R}^{N_r N_{v_\theta} \times N_x}$
 - 2: $\mathbf{Y} \leftarrow \text{unfold}(\mathbf{F}, (N_r, N_{v_\theta}, N_x))$ ▷ $\mathbf{Y} \in \mathbb{R}^{N_r \times N_{v_\theta} \times N_x}$
 - 3: $[\mathbf{Y}]_{ijk} \leftarrow [\mathbf{U}^{-1}]_{im} \times_m [\mathbf{F}^n]_{mjk}$ ▷ contraction on m index
 - 4: **for** $i \in \{0, \dots, N_r - 1\}$ **do**
 - 5: **for** $j \in \{0, \dots, N_{v_\theta} - 1\}$ **do**
 - 6: $\mathbf{Y}_{ijk} \leftarrow \mathbf{Q}_{ijkl} \times_l \mathbf{Y}_{ijl}$ ▷ $\mathbf{Q}_{ij} \in \mathbb{R}^{N_x \times N_x}$ and contraction on l index
 - 7: **end for**
 - 8: **end for**
 - 9: $[\mathbf{Y}]_{ijk} \leftarrow [\mathbf{U}]_{im} \times_m [\mathbf{F}^n]_{mjk}$ ▷ contraction on m index
 - 10: $\mathbf{F}^{1/2} \leftarrow \text{fold}(\mathbf{Y}, (N_r, N_{v_\theta} \times N_x))$ ▷ $\mathbf{F}^{1/2} \in \mathbb{R}^{N_r N_{v_\theta} \times N_x}$
 - 11: **return** $\mathbf{F}^{1/2}$
-

Algorithm 3.2 BTE velocity space operator action.

Require: $\mathbf{F} \in \mathbb{R}^{N_r N_{v_\theta} \times N_x}$, $\mathbf{E} \in \mathbb{R}_x^N$ – electric field, \mathbf{C}_{en} , \mathbf{A}_v , \mathbf{P}_O , \mathbf{P}_S , and Δt

Ensure: $\left(\mathbf{I}_{v, v_\theta} - \Delta t \mathbf{P}_O (\mathbf{C}_{en} + [\mathbf{E}]_i \mathbf{A}_v) \mathbf{P}_S \right) \mathbf{F}$ – operator action on \mathbf{F}

- 1: $\mathbf{F}_S \leftarrow \mathbf{P}_S \mathbf{F}$
 - 2: $\mathbf{F}_C \leftarrow \mathbf{C}_{en} \mathbf{F}_S$ and $\mathbf{F}_A \leftarrow \mathbf{A}_v \mathbf{F}_S$
 - 3: $\mathbf{G} \leftarrow \mathbf{F} - \Delta t \mathbf{P}_O (\mathbf{F}_C + \mathbf{E} \circ \mathbf{F}_A)$
 - 4: **return** \mathbf{G}
-

The semi-implicit approach has a timestep size restriction that arises from the decoupled electrostatics, spatial, and velocity space solves. This is determined by the BTE spatial advection and reaction timescales (see Subsection 3.4.1). To address this timestep size restriction, we propose a fully-implicit scheme for the BTE, which is

Algorithm 3.3 BTE velocity space GMRES preconditioner.

Require: \mathbf{F} , $\{\mathbf{H}_p\}_{p=1}^{N_c}$ – precondition operators, $\{w_p\}_{p=1}^{N_c}$ – domain decomposition, $\mathbf{P}_S, \mathbf{P}_O$

Ensure: Preconditioner action : $\mathbb{R}^{N_r N_{v_\theta} \times N_x} \rightarrow \mathbb{R}^{N_r N_{v_\theta} \times N_x}$

```

1:  $\mathbf{G} \leftarrow \mathbf{0}$ 
2:  $\mathbf{F}_S \leftarrow \mathbf{P}_S \mathbf{F}$ 
3: for  $p \in \{1, \dots, N_c\}$  do
4:    $\mathbf{G}[:, w_p] \leftarrow \mathbf{H}_p \mathbf{F}_S[:, w_p]$ 
5: end for
6:  $\mathbf{G} \leftarrow \mathbf{P}_O \mathbf{G}$ 
7: return  $\mathbf{G}$ 

```

$\triangleright \mathbf{G} \in \mathbb{R}^{N_r N_l \times N_x}$
 $\triangleright \mathbf{F}_S \in \mathbb{R}^{N_r N_l \times N_x}$
 $\triangleright \mathbf{G} \in \mathbb{R}^{N_r N_{v_\theta} \times N_x}$

given by

$$(3.35a) \quad \text{fully-implicit} \quad \begin{cases} \frac{\mathbf{F}^{n+1} - \mathbf{F}^n}{\Delta t} = -\mathbf{A}_x \mathbf{F}^{n+1} \mathbf{D}_x^T + \mathbf{P}_O \mathbf{C}_{en} \mathbf{P}_S \mathbf{F}^{n+1} + \\ \qquad \qquad \qquad \mathbf{P}_O \mathbf{A}_v \mathbf{P}_S (\mathbf{E}(\mathbf{F}^{n+1}) \circ \mathbf{F}^{n+1}), \\ (3.35b) \quad \mathbf{E}(\mathbf{F}) = \mathbf{L}(\mathbf{n}_i - \mathbf{u}^T \mathbf{F}). \end{cases}$$

We use Newton’s method with line search to solve the nonlinear system by Equation (3.35). The application of the Jacobian, evaluated at \mathbf{F} , on a given input \mathbf{X} is given by

$$(3.36) \quad \mathbf{J}_F \mathbf{X} = -\mathbf{A}_x \mathbf{X} \mathbf{D}_x^T + \mathbf{P}_O \mathbf{C}_{en} \mathbf{P}_S \mathbf{X} + \mathbf{P}_O \mathbf{A}_v \mathbf{P}_S (\mathbf{E}(\mathbf{F}) \circ \mathbf{X}) + \mathbf{P}_O \mathbf{A}_v \mathbf{P}_S (\mathbf{E}(\mathbf{X}) \circ \mathbf{F}).$$

Computing the linear step is, however, a challenge. If we try to assemble the Jacobian, we end up with a dense phase space operator with a prohibitive storage cost. Instead, we use a matrix-free GMRES solver, but it turns out the Jacobian is highly ill-conditioned. The solution is to use preconditioning. For this, we propose to use the linear operator corresponding to the update of the semi-implicit scheme defined in Equation (3.32) as a preconditioner. We discuss the efficiency of the solver in the results section.

3.4.3. Hybrid solver complexity. Recall that N_x , N_r , and N_{v_θ} denote the number of Chebyshev collocation points in position space, B-spline basis functions in v , and discrete ordinate points in v_θ . This will result in $N_x(1 + N_r N_{v_\theta})$ degrees of freedom for the hybrid solver. Recall, N_l denotes the number of spherical harmonics used for the mixed Galerkin and collocation discretization scheme used in v_θ coordinate. The velocity space operators \mathbf{C}_{en} , \mathbf{A}_v are stored as dense matrices. Operators \mathbf{A}_x , \mathbf{P}_S , \mathbf{P}_O are not assembled, and their actions are performed with tensor contractions with the stored \mathbf{D}_{v_θ} , \mathbf{G}_v , \mathbf{T}_S , and \mathbf{T}_O operators. These operators are stored as dense matrices. Table 3.4 summarizes all discretized BTE operators and their dimensions. It also provides the storage complexities for these operators and the computational complexity for their actions.

The computational complexities for $\mathbf{A}_x \mathbf{F} \mathbf{D}_x^T$ evaluation is given by $T_{\mathbf{x}\text{-rhs}} = \mathcal{O}(N_r N_{v_\theta} N_x (N_r + N_x))$, and the spatial advection solve in Algorithm 3.1 is $T_{\mathbf{x}\text{-solve}} = \mathcal{O}(N_r N_{v_\theta} N_x (N_r + N_x))$. The computation cost for $\mathbf{P}_O (\mathbf{C}_{en} + \mathbf{E} \circ \mathbf{A}_v) \mathbf{P}_S$ is $T_{\mathbf{v}\text{-rhs}} = \mathcal{O}((2N_{v_\theta} + N_r N_l) N_r N_l N_x)$. Application of the preconditioner has a similar costs so

Operator	Dimensions	Storage	Action on $\mathbf{X} \in \mathbb{R}^{N_r \times N_{v\theta} \times N_x}$, $\mathbf{X}_S \in \mathbb{R}^{N_r \times N_l \times N_x}$	Complexity
\mathbf{D}_x	$N_x \times N_x$	$\mathcal{O}(N_x^2)$	$[\mathbf{Y}]_{ijk} = [\mathbf{D}_x]_{im} \times_m [\mathbf{X}]_{jkm}$	$\mathcal{O}(N_x^2 N_r N_{v\theta})$
$\mathbf{A}_x = \mathbf{D}_{v\theta} \otimes \mathbf{G}_v$	$N_r N_{v\theta} \times N_r N_{v\theta}$	$\mathcal{O}(N_r^2 + N_{v\theta})$	$[\mathbf{Y}]_{ijk} = [D_{v\theta}]_{jj} \circ_j [\mathbf{G}_v]_{im} \times_m [\mathbf{X}]_{mjk}$	$\mathcal{O}(N_x N_{v\theta} N_r^2)$
$\mathbf{P}_S = \mathbf{I}_v \otimes \mathbf{T}_S$	$N_r N_l \times N_v N_{v\theta}$	$\mathcal{O}(N_{v\theta} N_l)$	$[\mathbf{Y}]_{ijk} = [\mathbf{T}_S]_{jm} \times_m [\mathbf{X}]_{imk}$	$\mathcal{O}(N_x N_r N_l N_{v\theta})$
$\mathbf{P}_O = \mathbf{I}_v \otimes \mathbf{T}_O$	$N_r N_{v\theta} \times N_r N_l$	$\mathcal{O}(N_{v\theta} N_l)$	$[\mathbf{Y}]_{ijk} = [\mathbf{T}_O]_{jm} \times_m [\mathbf{X}_S]_{imk}$	$\mathcal{O}(N_x N_r N_l N_{v\theta})$
\mathbf{C}_{en}	$N_r N_l \times N_r N_l$	$\mathcal{O}(N_r^2 N_l^2)$	$[\mathbf{Y}]_{ijk} = [\mathbf{C}_{en}]_{ijlm} \times_{lm} [\mathbf{X}_S]_{lmk}$	$\mathcal{O}(N_x N_r^2 N_l^2)$
\mathbf{A}_v	$N_r N_l \times N_r N_l$	$\mathcal{O}(N_r^2 N_l^2)$	$[\mathbf{Y}]_{ijk} = [\mathbf{A}_v]_{ijlm} \times_{lm} [\mathbf{X}_S]_{lmk}$	$\mathcal{O}(N_x N_r^2 N_l^2)$

Table 3.4: Summary of storage and computational complexity for the discretized BTE operators. Here \times_k denotes the contraction along index k , and \circ_k denotes element wise product along index k .

that $T_{v\text{-precond}} = T_{v\text{-rhs}}$. Hence, the overall computational cost for a single BTE time-step for the semi-implicit scheme is given by

$$(3.37) \quad T_{\text{semi-implicit}} = T_{\mathbf{x}\text{-solve}} + k(T_{v\text{-precond}} + T_{v\text{-rhs}}) = T_{\mathbf{x}\text{-solve}} + 2kT_{v\text{-rhs}}.$$

Here, $2kT_{v\text{-rhs}}$ denotes the velocity space GMRES solver cost, and k denotes the GMRES iterations for convergence. For the fully-implicit scheme, the right-hand side evaluation cost of the Jacobian action given in Equation (3.36) is $T_{v\mathbf{x}\text{-jac}} = T_{\mathbf{x}\text{-rhs}} + T_{v\text{-rhs}} + T_{\mathbf{E}\text{-solve}}$. Here, \mathbf{E} solve cost is $T_{\mathbf{E}\text{-solve}} = \mathcal{O}(N_r N_{v\theta} N_x + N_x^2)$, and since $(T_{\mathbf{x}\text{-rhs}} + T_{v\text{-rhs}}) \gg T_{\mathbf{E}\text{-solve}}$ it is omitted in the analysis. The operator split preconditioning cost for the fully implicit scheme is $T_{v\mathbf{x}\text{-precond}} = T_{\mathbf{x}\text{-rhs}} + T_{v\text{-rhs}}$. Taken together, the computational complexity for a single timestep solve of the fully-implicit scheme is given by

$$(3.38) \quad T_{\text{fully-implicit}} = k(T_{v\mathbf{x}\text{-precond}} + T_{v\mathbf{x}\text{-jac}}) = 2k(T_{\mathbf{x}\text{-rhs}} + T_{v\text{-rhs}}).$$

Here, k denotes the total Newton-GMRES iterations for convergence. Let $(\Delta t_F, k_F)$ and $(\Delta t_S, k_S)$ tuples denote the timestep size and the number of iterations for the described fully-implicit and semi-implicit schemes respectively. The cost ratio S of the semi-implicit to fully-implicit scheme is given by

$$(3.39) \quad \frac{\Delta t_F (T_{\mathbf{x}\text{-rhs}} + 2k_S T_{v\text{-rhs}})}{\Delta t_S 2k_F (T_{\mathbf{x}\text{-rhs}} + T_{v\text{-rhs}})}.$$

Due to the nonlinearity and ill-conditioning of Equation (3.35) it is hard to determine the effectiveness of the fully-implicit scheme. It depends on the preconditioned linear solves and the underlying prefactors in the complexity estimates, some of which are related to memory accesses and hardware performance. Next, we describe a series of numerical experiments to compare the two schemes.

3.5. Implementation. We have implemented all the presented algorithms in Python and we release them in a library we call BOLTZSIM. We use NumPy and CuPy libraries for all the linear algebra operations. The above libraries provide an interface to basic linear algebra subprograms (BLAS) for CPU and GPU architectures. Both hybrid and the fluid model time integration supports GPU acceleration with CuPy. We use CuPy GMRES solver with `LinearOperator` class to specify operator and preconditioner actions. The batched GEMM operations are performed using the `einsum` function. BOLTZSIM is available at <https://github.com/ut-padas/boltzmann.git>.

4. Results. We organize the results as follows. Subsection 4.1 presents a self-convergence study for the developed Eulerian BTE solver and cross-verification comparison with an in-house PIC-DSMC code. Performance evaluation of the developed algorithms is presented in Subsection 4.2. Subsection 4.3 presents a detailed comparison study between the hybrid and the fluid approximations of RF-GDPs for different pressure regimes.

4.1. Boltzmann transport with specified electric field. We consider the electron BTE with zero incoming flux boundary conditions as specified by Equations (3.16b) and (3.16g).

We evolve this equation with the initial conditions described by

$$(4.1) \quad f(t=0, x, \mathbf{v}) = \frac{n_e(t=0, x)}{\pi^{3/2} v_{th}^3} \exp\left(-\left(\frac{\|\mathbf{v}\|_2}{v_{th}}\right)^2\right) \text{ where,}$$

$$n_e(t=0, x) = 10^{13} + 10^{15}(1-x/L)^2(x/L)^2 \text{ [m}^{-3}\text{]}, \quad v_{th} = \sqrt{\frac{2k_B T_e}{m_e}} \text{ and } T_e = 0.5\text{eV,}$$

with a specified electric field $E(x, t)$. The electric field causes electron acceleration along the opposite direction, triggering ionization events. Hence, we observe oscillatory growth of electron number density.

Convergence: We use this problem to perform a convergence study. We consider a time-harmonic spatially homogeneous electric field given by $E(x, t) = 10^4 \sin(2\pi\zeta t)$ [V/m] with $\zeta = 13.56\text{MHz}$. Table 4.1 summarizes the parameters used for the convergence study. Figure 4.1 shows the convergence of the evolved solution with increasing resolution in the phase space. Figures 4.1a to 4.1c show the oscillatory growth of the electron number density $n_e(x)$, Figures 4.1d to 4.1f show the relative errors of $n_e(x)$ with respect to the highest resolution run, and Figures 4.1g to 4.1i show the convergence of the electron energy density function at a chosen spatial location.

run id	N_x	N_r	N_{v_θ}	N_l	$\frac{\Delta t}{(1/\zeta)}$
r_0	100	128	16	2	5e-4
r_1	200	256	32	4	2e-4
r_2	200	512	64	8	1e-4

Table 4.1: Refinement parameters used in space, velocity space and time for the convergence study presented in Figure 4.1.

We solve the electron BTE given in Equations (3.16b) and (3.16g) with our BOLTZSIM and PIC-DSMC codes and we report the results in Figure 4.2. The results show excellent agreement between the two solvers.

4.2. Performance evaluation. We summarize performance evaluation results for the fluid and BOLTZSIM solvers for RF-GDPs. We conducted our experiments on Lonestar 6 at the Texas Advanced Computing Center (TACC). Each node on Lonestar 6 has two AMD EPYC 7763 CPUs and three NVIDIA A100 GPUs. The presented fluid and BOLTZSIM performance results are conducted on a single AMD EPYC 7763 CPU core and a single NVIDIA A100 GPU. Table 4.2 summarizes the overall implicit timestep cost for the fluid solver. We observe $\mathcal{O}(N_x^3)$ growth of the timestep cost

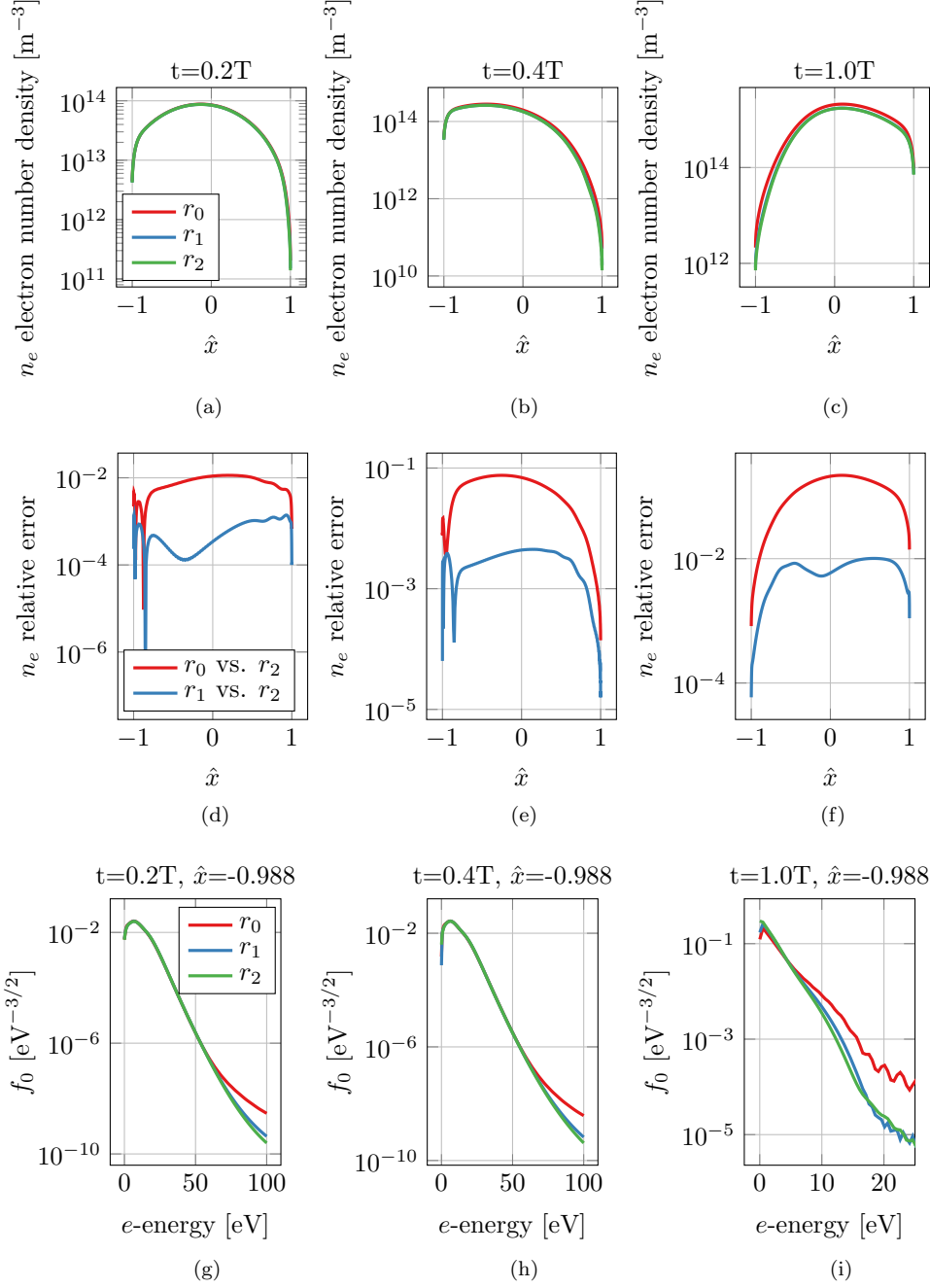


Fig. 4.1: Electron transport using BTE with specified electric field $E(x, t) = 10^4 \sin(2\pi\zeta t)$ with $\zeta = 13.56\text{MHz}$. Figures 4.1a to 4.1c show the electron number density $n_e(x) = \int_{\mathbf{v}} f(x, \mathbf{v}) d\mathbf{x}$ evolution in time for runs r_0 , r_1 , and r_2 specified in Table 4.1. Figures 4.1d to 4.1f show relative error in $n_e(x)$ with respect to the highest resolution run r_2 . Figures 4.1g to 4.1i show the electron energy density function at spatial location $(2x/L - 1) = \hat{x} = -0.988$ for subsequent runs r_0 , r_1 and r_2 .

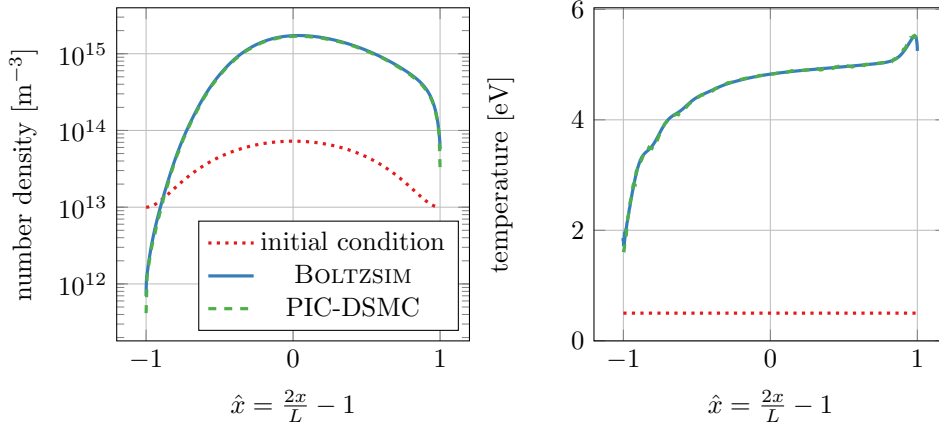


Fig. 4.2: We consider the electron BTE given in Equations (3.16b) and (3.16g) with electric field $E(x, t) = 10^4 \sin(2\pi\zeta t)$ with $\zeta = 13.56\text{MHz}$. The figure shows solutions after a one period $1/f$. The blue line is BOLTZSIM and the broken green line is PIC-DSMC.

N_x	$\Delta t/(1/\zeta)$	timestep (s)
100	1.00E-03	9.0785E-03
200	1.00E-03	2.9685E-02
400	1.00E-03	1.7288E-01

Table 4.2: The fluid solver runtime for a single implicit timestep with increasing spatial resolution. The above results are conducted using a single core of AMD EPYC 7763 CPU .

where N_x denotes the number of Chebyshev collocation points in space. This is due to the direct Jacobian factorization used in the Newton iteration.

Performance evaluation results of the BOLTZSIM solver is presented in Table 4.3. Here, N_x , N_r , N_{v_θ} , and N_l denote the number of Chebyshev collocation points in the position space, B-spline basis functions in speed, discrete ordinate points, and spherical basis functions are used in v_θ . For coarser spatial grids, we observe that the fully-implicit scheme is $\sim 2\times$ faster than the semi-implicit scheme. With increased spatial resolution, the fully-implicit scheme becomes more expensive than the semi-implicit scheme. This is primarily due to the increased $T_{\mathbf{x}\text{-rhs}}$ cost. Recall that the complexities of fully-implicit and semi-implicit schemes are given by $2k(T_{\mathbf{x}\text{-rhs}} + T_{\mathbf{v}\text{-rhs}})$ and $(T_{\mathbf{x}\text{-rhs}} + 2kT_{\mathbf{v}\text{-rhs}})$ where k denotes the number of iterations for convergence. Hence, the increased $T_{\mathbf{x}\text{-rhs}}$ reduces the overall efficiency of the fully-implicit scheme. Of course both methods are orders of magnitude faster than an explicit method. We use the coarse grid fully-implicit scheme to march over the transient and reach the time-periodic state. Once time-periodicity is reached, we use iterative refinement with semi-implicit time integration to resolve the finer features of the time-periodic state.

Figure 4.3 shows the overall cost breakdown for a single timestep for evolving the hybrid formulation of RF-GDPs with semi-implicit and fully-implicit time integration schemes. We compute these percentages based on each method's overall runtime for

N_r	$N_{v\theta}$	N_l	N_x	$\Delta t_S \times f$	$\Delta t_F \times f$	semi-implicit (s)	fully-implicit (s)	speedup
64	16	3	100	5E-05	2E-04	3.53E-02	6.52E-02	2.1x
128	16	3	100	5E-05	2E-04	3.61E-02	6.55E-02	2.2x
256	16	3	100	5E-05	2E-04	3.71E-02	6.68E-02	2.2x
64	16	3	100	5E-05	2E-04	3.53E-02	6.52E-02	2.1x
128	16	3	200	5E-05	2E-04	3.93E-02	2.52E-01	0.6x
256	16	3	400	5E-05	2E-04	6.37E-02	–	–

Table 4.3: Comparison of the overall timestep cost for the BOLTZSIM solver using semi-implicit and fully-implicit schemes. Although the fully implicit solver is more expensive per timestep, it is faster overall because it requires fewer timesteps. The last column shows the overall runtime (semi-implicit / fully-implicit). The fully-implicit scheme is $\sim 2\times$ faster than the semi-implicit scheme for coarser spatial grids $N_x=100$. For $N_x \geq 200$ the fully-implicit solve becomes too expensive.

a single complete timestep to evolve ions and electrons. Even though the relative cost of the BTE update is 10% higher in the fully-implicit scheme, compared to the semi-implicit approach, it allows larger timestep sizes that respect timescales of ions.

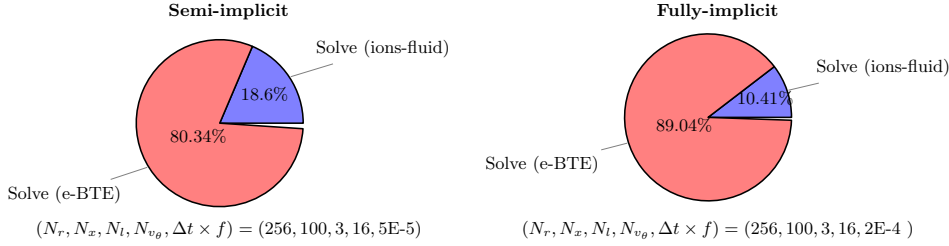


Fig. 4.3: The overall runtime cost breakdown for a single RF-GDP timestep using the hybrid modeling approach. The left and right plots show the cost breakdown using semi-implicit and fully-implicit schemes for evolving the electron BTE. In both cases, \mathbf{E} -field solve cost is negligible compared to others, hence omitted in the plot.

4.3. Glow discharge. For modeling RF-GDPs, we present a comparative study of the fluid and the hybrid approaches, which are given by Equations (3.15) and (3.16). The key difference between the fluid and hybrid modeling approaches is how the electron transport is being modeled. The fluid approach transports electrons and ions using fluid equations. In contrast, in the hybrid model, electron transport is kinetic by solving the BTE, while we use the standard fluid transport for ions. We consider four cases with varying gas pressure values ranging from 0.1 Torr to 2 Torr while keeping other parameters unchanged. Since $n_0 \sim \frac{p_0}{k_B T}$, lower pressure values result in lower background number densities. This causes the plasma to be less collisional. Our primary goal is to identify the modeling discrepancies between hybrid and fluid-based electron transport under different pressure regimes. The simulation parameters used for the study are summarized in Table 4.4. The fluid approximation-based species transport relies on a closure model for kinetic coefficients. The simplest closure model would be the Maxwellian EDF assumption and derive temperature-based electron kinetic coefficients [13]. The above is not ideal due to the electric field

Parameter	Symbol	Value	Reference
Gas pressure	p_0	0.1Torr, 0.5Torr, 1Torr, 2Torr	–
Gas temperature	T_0	300 K	–
Neutral density	n_0	$(0.322, 1.61, 3.22, 6.44) \times 10^{22} \text{m}^{-3}$	ideal gas law
Electrode gap	L	$2.54 \times 10^{-2} \text{ m}$	[13]
Peak voltage	V_0	100 V	[13]
Oscillation frequency	f	13.56 MHz	[15]
Electron diffusion	D_e	BOLSIG+ (0D-BTE)	[9, 8]
Ion diffusion	D_i	$n_0 D_i = 2.07 \times 10^{20} \text{m}^{-1} \text{s}^{-1}$	[15]
Electron mobility	μ_e	BOLSIG+ (0D-BTE)	[9, 8]
Ion mobility	μ_i	$n_0 \mu_i = 4.65 \times 10^{21} \text{V}^{-1} \text{m}^{-1} \text{s}^{-1}$	[15]
$e + Ar \rightarrow 2e + Ar^+$	k_i	BOLSIG+ (0D-BTE)	[9, 8]

Table 4.4: Modeling parameters used in the presented work.

effects in RF-GDPs and other LTPs because of strong deviation from Maxwellian and non-local effects that can occur at low pressures. In our fluid approximation, we allow non-Maxwellian treatment of kinetic coefficients by solving spatially homogeneous electron BTE. We use the state-of-the-art BOLSIG+ framework [9] to compute steady-state EDFs for varying $\|\mathbf{E}\|$ values with corresponding neutral density n_0 and gas temperature T_0 . With the computed steady-state EDFs, we build electron temperature-based look-up tables for required electron kinetics. The above process is illustrated in Figure 4.4. Figure 4.5 shows the tabulated kinetic coefficients plotted against the electron temperature T_e . Following [13] we use constant D_i, μ_i for ions.

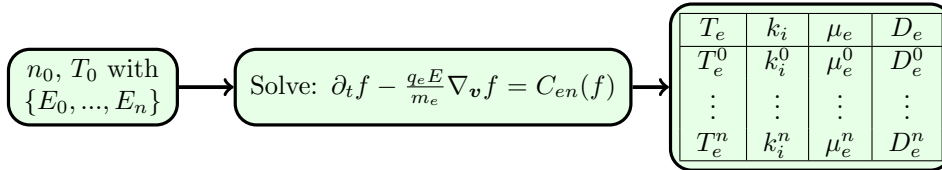


Fig. 4.4: An illustrative diagram that describes the process of computing tabulated kinetic coefficients for electrons to be used in the fluid model (Equation 3.15). For a fixed n_0, T_0 , we compute the steady-state EDF solutions for the spatially homogeneous BTEs for a given electric field values i.e., $\{E_0, \dots, E_n\}$. For each E_j , we compute kinetic coefficients $\{k_i^j, \mu_e^j, D_e^j\}$ and corresponding temperature T_e^j . Then for example, for μ_e , we build an interpolant $\mu_e(T_e)$ using the $\{\mu_e^j, T_e^j\}$ pairs.

For RF-GDPs, the time-periodic steady-state solution is determined by the background gas temperature T_0 , pressure p_0 , the electrode gap L , and the peak driving voltage V_0 . As mentioned, we consider the p_0 values listed in Table 4.4 while keeping all other parameters fixed. Changing p_0 changes the neutral density n_0 , which is coupled to the problem through electron-heavy binary collisions and heavy species kinetic coefficients.

Both hybrid and fluid solvers were time-marched until the time-periodic state is achieved. We compute the time-periodic solution from the fluid solver with initial conditions given by [15]. This solution is then used as an initial condition for the

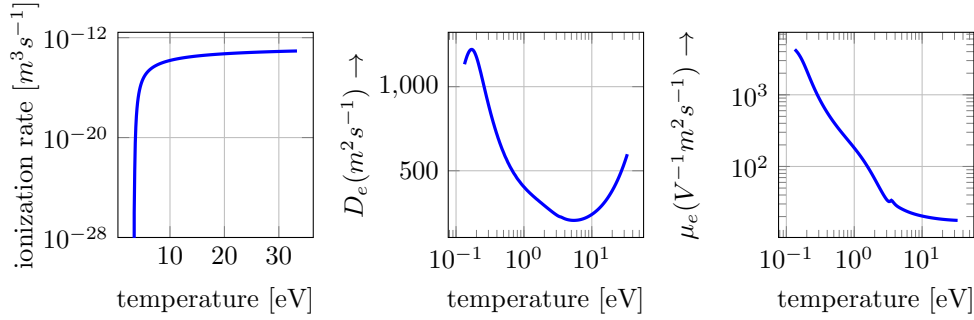


Fig. 4.5: Tabulated electron kinetic coefficients based on the steady-state solutions of the 0D3V electron BTE.

hybrid solver, where the EDFs are initialized as Maxwellian distributions defined by the temperature computed by the fluid solver.

p_0 [Torr]	Hybrid - cycle averaged peak			Fluid - cycle averaged peak		
	n_e [m^{-3}]	ε_e [eVkgm $^{-3}$]	$ E $ [V/m]	n_e [m^{-3}]	ε_e [eVkgm $^{-3}$]	$ E $ [V/m]
0.1	4.27E+16	5.65E-14	2.32E+04	5.87E+14	3.660E-15	1.27E+04
0.5	2.51E+16	5.33E-14	3.15E+04	8.18E+15	4.35E-14	3.23E+04
1.0	4.06E+16	1.10E-13	4.44E+04	2.51E+16	1.31E-13	4.83E+04
2.0	7.67E+16	1.72E-13	5.32E+04	7.79E+16	3.98E-13	7.06E+04

Table 4.5: A summary of the peak values for the cycle-averaged time-periodic steady-state profiles computed by fluid and hybrid modeling approaches.

The cycle-averaged profiles are shown in Figure 4.6. Table 4.5 summarizes the peak values for the cycle-averaged time-periodic solutions computed by fluid and hybrid models. For the cycle-averaged profiles, the largest discrepancy between the fluid and the hybrid model is reported in the lowest pressure case, $p_0 = 0.1$ Torr. Specifically, the hybrid computed peak cycle-averaged steady-state electron number density is 80x, 3x, and 1.6x higher compared to the equivalent fluid runs for 0.1 Torr, 0.5 Torr, and 1 Torr cases. For the highest pressure case presented, $p_0 = 2$ Torr, the cycle-averaged electron number density profiles agree quite well but there are still discrepancies, for example the peak electric field. Below we list the reasons that contribute to this discrepancies.

Tabulated rate coefficients: The fluid approximation of the RF-GDPs relies on a closure model for the electron kinetic coefficients. In the fluid solve, electron kinetics are computed using tabulated results using the 0D3V BTE while for hybrid model, kinetics coefficients are computed by the 1D3V BTE. Figure 4.8 shows the radial components of the cycle-averaged steady-state EDFs computed by the hybrid solver. With increasing background gas pressure, the EDFs at the center of the discharge show rapidly depleted tails at the ionization energy threshold value 15.76 eV. Specifically, for the 0.1 Torr case, tails are more prominent due to reduced collisionality. Similarly, the anisotropic correction modes are dominant compared to runs with higher background gas pressure. Furthermore, tabulated data-based kinetic coefficients are inaccurate for low-pressure cases because the 0D3V BTE misses spatial coupling effects. These effects become more pronounced with decreasing pressure.

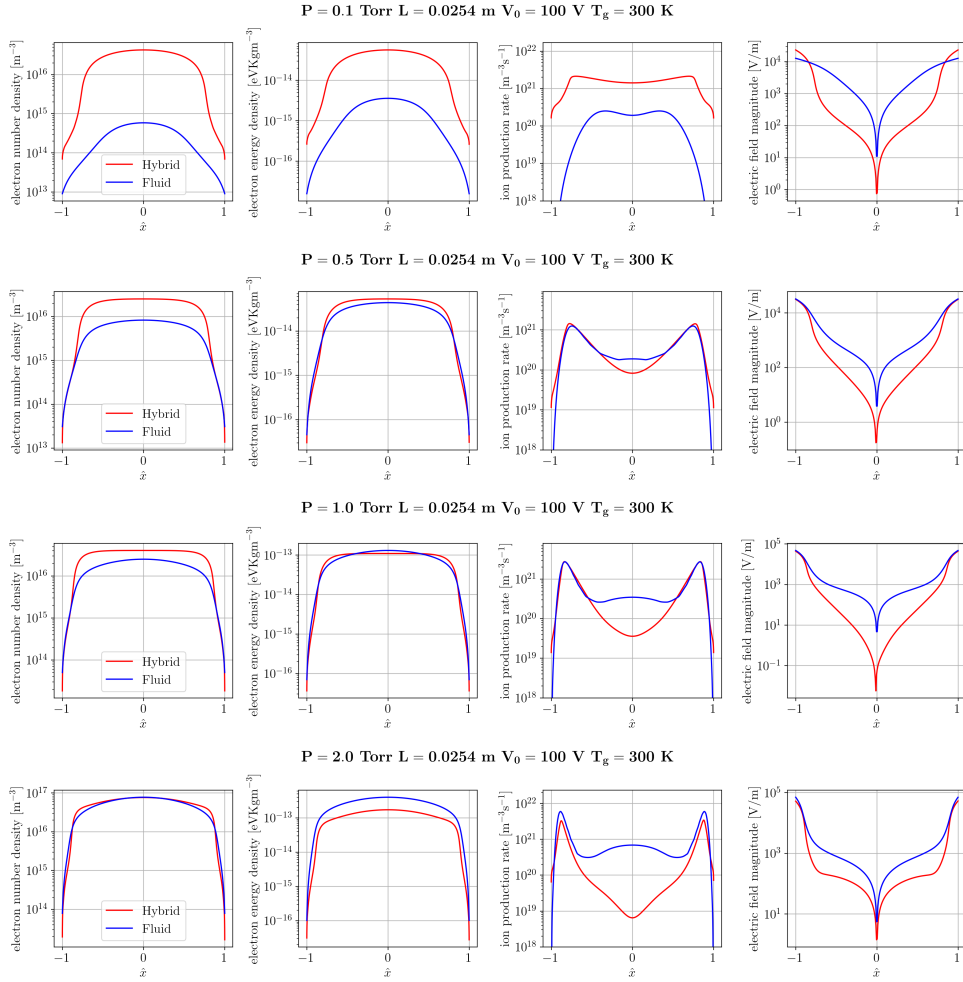


Fig. 4.6: Cycle-averaged time-periodic steady-state profiles computed by the hybrid and the fluid approximation of RF-GDPs under varying pressure values from 0.1 Torr to 2 Torr.

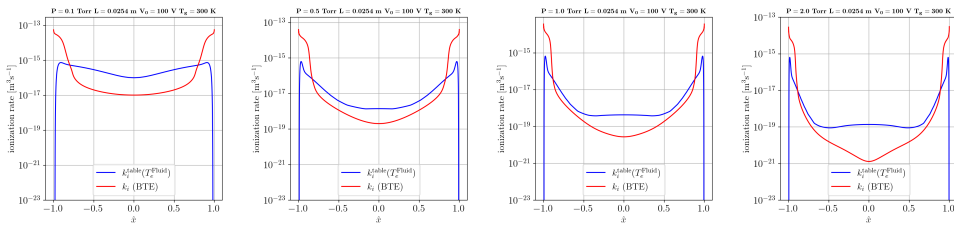


Fig. 4.7: Discrepancies in the ionization rate coefficient computed from the tabulated data generated from steady-state spatially homogeneous BTE and spatially coupled BTE in the hybrid modeling approach.

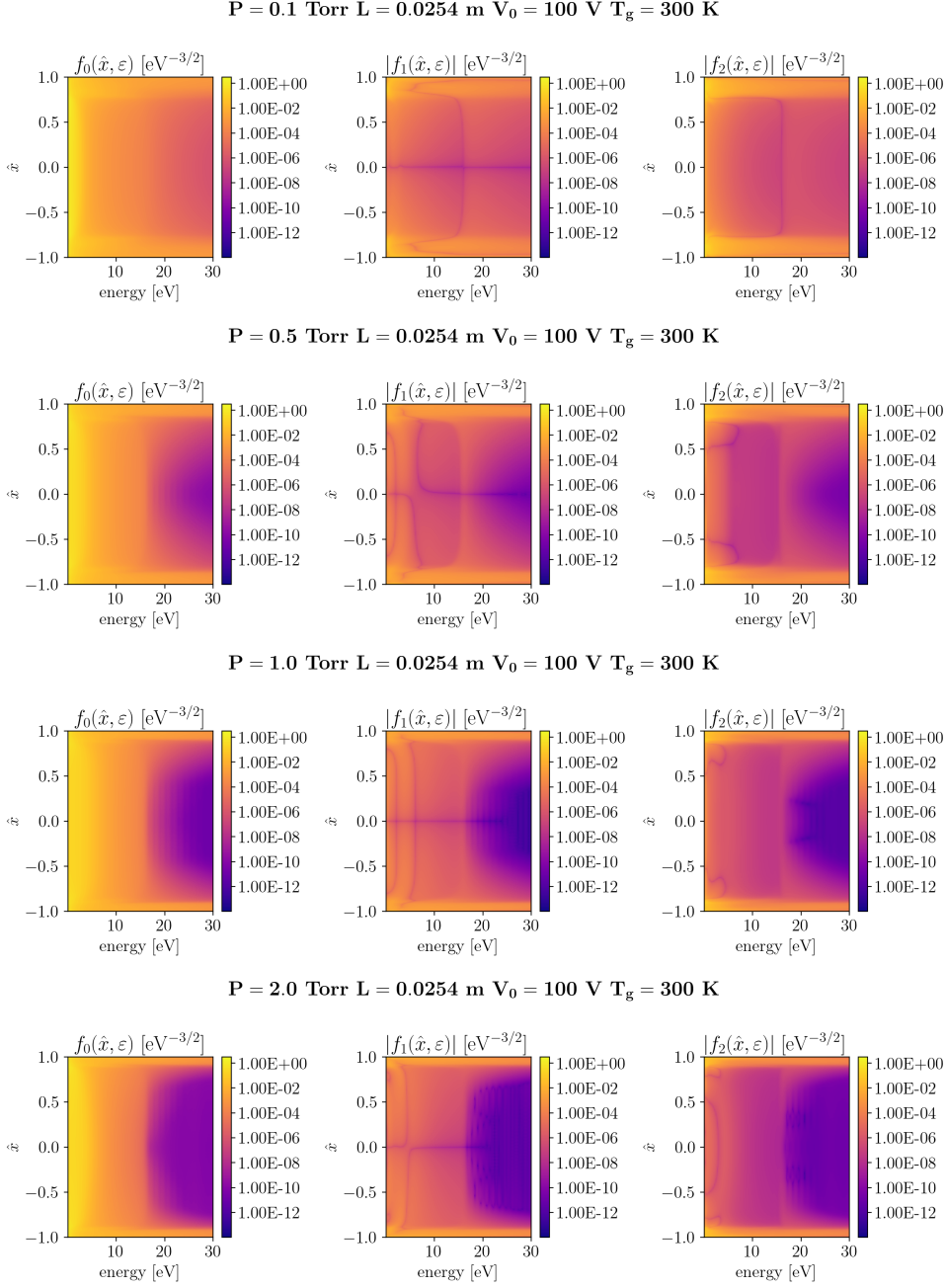


Fig. 4.8: Cycle-averaged time-periodic steady-state EDF solutions in RF-GDPs for the different pressure values computed using the hybrid modeling approach.

The drift-diffusion approximation: The fluid model uses the drift-diffusion approximation to derive a closed expression for the electron flux term \mathbf{J}_e . The drift-diffusion approximation assumes that the EDFs are isotropic and electron drift veloc-

ity is negligible compared to the collisional momentum transfer frequency. Figure 4.9 shows the cycle-averaged electron drift velocity computed by the hybrid and the fluid modeling approaches. At the sheath region, we observe higher relative errors, greater than 1%, compared to the center. Due to the large electric field effects, the EDFs at the sheath regions depict higher anisotropic effects compared to the discharge center (see Figure 4.8). Therefore, the drift-diffusion approximation becomes less valid at the sheath regions and has larger errors compared to the discharge center.

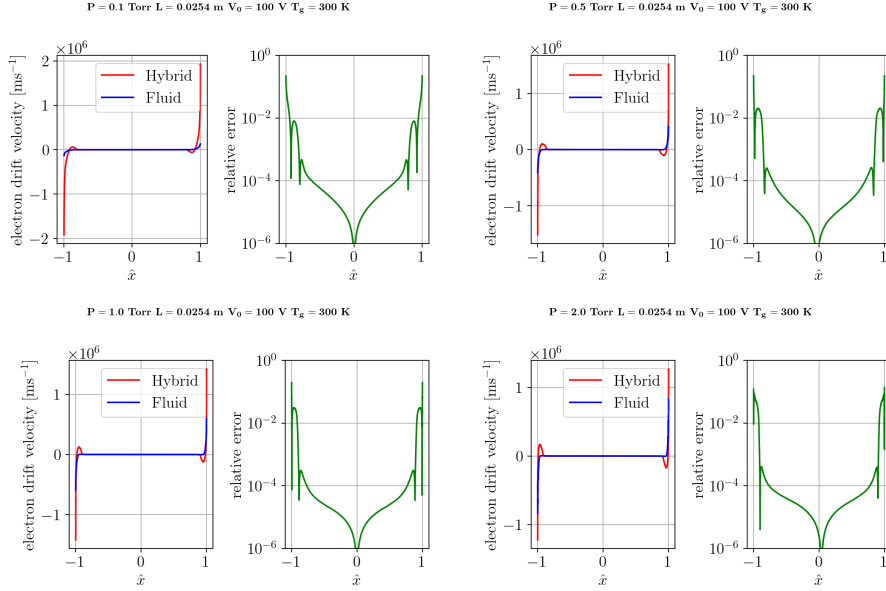


Fig. 4.9: Comparison of the cycle-averaged electron drift velocity computed based on the hybrid and the fluid approximation modeling approaches. The second column for each case shows the relative error between the two approaches taking the hybrid model as the true solution with respect to its l_2 norm.

Boundary conditions: For the hybrid approximation, we use zero incoming flux boundary conditions for the electrons. This will cause non-Maxwellian EDFs at the discharge walls. In contrast, the fluid approximation assumes Maxwellian EDF at discharge walls. Specifically, for the fluid model, the electron boundary flux term is derived based on the Maxwellian EDF assumption, and it is non-linearly coupled to the electron energy equation. The above discrepancy in the boundary EDF between the models also contributes to the differences we observe in the steady-state profiles.

5. Conclusions. We presented the BOLTZSIM solver for the one-dimensional electron BTE for LTPs. BOLTZSIM uses a Eulerian approach with a Chebyshev-collocation in the position space. In the velocity space, we use a Galerkin discretization in the radial direction and a mixed spherical harmonics with discrete ordinate method for the angular directions. We compare two models for electron transport, fluid and BTE. In the fluid approximation, we rely on the continuity equations for species transport. For the hybrid approximation, we use continuity equations for ions while using the BTE for electron transport. In the fluid approximation, we use non-Maxwellian treatment of EDFs with tabulated kinetic coefficients. As expected, at

lower pressures, we observe significant differences between the time-periodic profiles, computed based on the fluid and hybrid approximations. The above indicates that the kinetic treatment of electrons is crucial for accurate RF-GDPs simulation, and the widely-used tabulated interpolation of kinetic coefficients is inadequate to capture the spatial coupling effects on EDFs.

6. Future work. We plan to explore electron transport differences with more heavy species, especially meta-stables and excited species. Both fluid and hybrid approaches require long time horizons with thousands of RF cycles to achieve time-periodic solutions. The above can be eliminated by a reduce-order model that can generate approximate time-periodic solutions, and the above can be used as an initial condition for the high-fidelity model. Another possible extension would be to explore spatially adaptive velocity space discretization. This can benefit greatly, especially moving towards solving the 3D3V BTE.

REFERENCES

- [1] M. S. BARNES, T. J. COTLER, AND M. E. ELTA, *A staggered-mesh finite-difference numerical method for solving the transport equations in low pressure rf glow discharges*, Journal of Computational physics, 77 (1988), pp. 53–72.
- [2] T. J. BARTEL, *Modelling neutral & plasma chemistry with dsmc*, in AIP Conference Proceedings, vol. 663, American Institute of Physics, 2003, pp. 849–856.
- [3] J.-P. BOEUF, *Numerical model of rf glow discharges*, Physical review A, 36 (1987), p. 2782.
- [4] A. BOGAERTS, R. GIJBELS, AND W. WIMGOEDHEER, *Hybrid modeling of a capacitively coupled radio frequency glow discharge in argon: Combined monte carlo and fluid model*, Japanese journal of applied physics, 38 (1999), p. 4404.
- [5] P. G. CIARLET, *The finite element method for elliptic problems*, SIAM, 2002.
- [6] M. FERNANDO, D. BOCHKOV, J. ALMGREN-BELL, T. OLIVER, R. MOSER, P. VARGHESE, L. RAJA, AND G. BIROS, *A fast solver for the spatially homogeneous electron boltzmann equation*, 2024, <https://arxiv.org/abs/2409.00207>, <https://arxiv.org/abs/2409.00207>.
- [7] A. FREZZOTTI, G. P. GHIROLDI, AND L. GIBELLI, *Solving the boltzmann equation on gpus*, Computer Physics Communications, 182 (2011), pp. 2445–2453.
- [8] G. HAGELAAR, *Coulomb collisions in the boltzmann equation for electrons in low-temperature gas discharge plasmas*, Plasma Sources Science and Technology, 25 (2015), p. 015015.
- [9] G. HAGELAAR AND L. C. PITCHFORD, *Solving the boltzmann equation to obtain electron transport coefficients and rate coefficients for fluid models*, Plasma sources science and technology, 14 (2005), p. 722.
- [10] T. L. HILL, *An introduction to statistical thermodynamics*, Courier Corporation, 1986.
- [11] P. KOTHNUR AND L. RAJA, *Simulation of direct-current microdischarges for application in electro-thermal class of small satellite propulsion devices*, Contributions to Plasma Physics, 47 (2007), pp. 9–18.
- [12] D. LEVKO, R. R. UPADHYAY, A. KARPATNE, D. BREDEN, K. SUZUKI, V. TOPALIAN, C. SHUKLA, AND L. L. RAJA, *VizGrain: a new computational tool for particle simulations of reactive plasma discharges and rarefied flow physics*, Plasma Sources Science and Technology, 30 (2021), p. 055012.
- [13] Q. LIU, Y. LIU, T. SAMIR, AND Z. MA, *Numerical study of effect of secondary electron emission on discharge characteristics in low pressure capacitive rf argon discharge*, Physics of Plasmas, 21 (2014).
- [14] D. LOFFHAGEN AND F. SIGENEGER, *Advances in boltzmann equation based modelling of discharge plasmas*, Plasma Sources Science and Technology, 18 (2009), p. 034006.
- [15] D. P. LYMBEROPOULOS AND D. J. ECONOMOU, *Fluid simulations of glow discharges: Effect of metastable atoms in argon*, Journal of applied physics, 73 (1993), pp. 3668–3679.
- [16] D. P. LYMBEROPOULOS AND J. D. SCHIEBER, *Stochastic dynamic simulation of the boltzmann equation for electron swarms in glow discharges*, Physical Review E, 50 (1994), p. 4911.
- [17] G. OBLAPENKO, D. GOLDSTEIN, P. VARGHESE, AND C. MOORE, *A velocity space hybridization-based boltzmann equation solver*, Journal of Computational Physics, 408 (2020), p. 109302.
- [18] P. K. PANNEER CHELVAM AND L. L. RAJA, *Computational modeling of the effect of external electron injection into a direct-current microdischarge*, Journal of Applied Physics, 118 (2015).

- [19] L. C. PITCHFORD, L. L. ALVES, K. BARTSCHAT, S. F. BIAGI, M.-C. BORDAGE, I. BRAY, C. E. BRION, M. J. BRUNGER, L. CAMPBELL, A. CHACHEREAU, ET AL., *Lxcat: An open-access, web-based platform for data needed for modeling low temperature plasmas*, Plasma Processes and Polymers, 14 (2017), p. 1600098.
- [20] K. S. K. SATAKE, T. M. T. MONAKA, O. U. O. UKAI, Y. T. Y. TAKEUCHI, AND M. M. M. MURATA, *Two-dimensional nonequilibrium plasma modeling based on the particle-boltzmann hybrid model for rf glow discharges*, Japanese journal of applied physics, 36 (1997), p. 4789.
- [21] T. SCANLON, E. ROOHI, C. WHITE, M. DARBANDI, AND J. REESE, *An open source, parallel dsmc code for rarefied gas flows in arbitrary geometries*, Computers & Fluids, 39 (2010), pp. 2078–2089.
- [22] M. SURENDRA AND D. B. GRAVES, *Particle simulations of radio-frequency glow discharges*, IEEE transactions on plasma science, 19 (1991), pp. 144–157.
- [23] L. TSENDIN, *Electron kinetics in non-uniform glow discharge plasmas*, Plasma Sources Science and Technology, 4 (1995), p. 200.
- [24] M. H. WILCOXSON AND V. I. MANOUSIOUTHAKIS, *Simulation of a three-moment fluid model of a two-dimensional radio frequency discharge*, Chemical engineering science, 51 (1996), pp. 1089–1106.
- [25] F. F. YOUNG ET AL., *A comparative study between non-equilibrium and equilibrium models of rf glow discharges*, Journal of Physics D: Applied Physics, 26 (1993), p. 782.
- [26] F. F. YOUNG AND C.-H. WU, *Two-dimensional, self-consistent, three-moment simulation of rf glow discharge*, IEEE transactions on plasma science, 21 (1993), pp. 312–321.
- [27] C. YUAN, E. BOGDANOV, S. ELISEEV, AND A. KUDRYAVTSEV, *1d kinetic simulations of a short glow discharge in helium*, Physics of Plasmas, 24 (2017).
- [28] S. ZABELOK, R. ARSLANBEKOV, AND V. KOLOBOV, *Adaptive kinetic-fluid solvers for heterogeneous computing architectures*, Journal of Computational Physics, 303 (2015), pp. 455–469.
- [29] L.-L. ZHAO, Y. LIU, AND T. SAMIR, *Numerical study on discharge characteristics influenced by secondary electron emission in capacitive rf argon glow discharges by fluid modeling*, Chinese Physics B, 27 (2018), p. 025201.